

1 **Source Sector and Region Contributions to BC and PM_{2.5} in Central Asia**

2 S. Kulkarni^{1*}, N. Sobhani^{1,2}, J. P. Miller-Schulze^{3,4}, M. M. Shafer^{3,4}, J. J. Schauer^{3,4}, P. A.
3 Solomon⁵, P. E. Saide¹, S. N. Spak^{6,1}, Y. F. Cheng^{1**}, H.A.C. Denier van der Gon⁷, Z. Lu⁸, D.G.
4 Streets⁸, G. Janssens-Maenhout⁹, C. Wiedinmyer¹⁰, J. Lantz¹¹, M. Artamonova¹², B. Chen¹³, S.
5 Imashev¹³, L. Sverdlik¹³, J. T. Deminter³, B. Adhikary^{1***}, A. D'Allura¹⁴, C. Wei^{1****}, and G. R.
6 Carmichael^{1,2}

7 ¹Center for Global and Regional Environmental Research, University of Iowa, Iowa City, IA

8 ²Department of Chemical & Biochemical Engineering, The University of Iowa, Iowa City, IA
9 52242, USA

10 ³ Wisconsin State Laboratory of Hygiene, 2601 Agriculture Drive, Madison, WI 53718, USA

11 ⁴ Environmental Chemistry and Technology Program, 660 North Park St, University of
12 Wisconsin, Madison, WI 53706, USA

13 ⁵ U.S. EPA, Office of Research & Development, Las Vegas, NV 89193, USA

14 ⁶ Public Policy Center, University of Iowa, 223 South Quadrangle, Iowa City, IA 52242

15 ⁷ TNO, Princetonlaan 6, 3584 CB Utrecht, The Netherlands

16 ⁸ Decision and Information Sciences Division, Argonne National Laboratory, Argonne, IL, USA

17 ⁹ European Commission, Joint Research Centre, IES, 21027 Ispra, Italy

18 ¹⁰ National Center for Atmospheric Research, Boulder, Colorado, USA

19 ¹¹ U.S. EPA, Office of Radiation and Indoor Air, Las Vegas, NV 89193, USA

20 ¹² Institute of Atmospheric Physics, 109017 Moscow, Russia

21 ¹³ Kyrgyz-Russian Slavic University, 44 Kievskaya Str., Bishkek 720000, Kyrgyzstan

22 ¹⁴ ARIANET, via Gilino 9, 20128 Milan, Italy

23 * now at: California Air Resource Board, Sacramento, CA USA

24 **now at: Multiphase chemistry department, Max Planck Institute for Chemistry, Mainz 55128,
25 Germany

26 *** now at: International Centre for Integrated Mountain Development (ICIMOD), GPO Box
27 3226, Kathmandu, Nepal

28 ****now at US EPA, Atmospheric Modeling and Analysis Division, Research Triangle Park,
29 NC USA

30 Correspondence to: N. Sobhani (negin-sobhani@uiowa.edu) and G.R. Carmichael
31 (gcarmich@engineering.uiowa.edu)

32

33 **Abstract**

34 Particulate matter (PM) mass concentrations, seasonal cycles, source sector and source region
35 contributions in Central Asia (CA) are analyzed for the period April 2008-July 2009 using the
36 Sulfur Transport and dEposition Model (STEM) chemical transport model and modeled
37 meteorology from the Weather Research and Forecasting (WRF) model. Predicted Aerosol
38 Optical Depth (AOD) values (annual mean value ~ 0.2) in CA vary seasonally with lowest values
39 in the winter. Surface $PM_{2.5}$ concentrations (annual mean value $\sim 10 \mu\text{g}/\text{m}^3$) also exhibit a
40 seasonal cycle, with peak values and largest variability in the spring/summer, and lowest values
41 and variability in the winter (hourly values from 2 – 90 $\mu\text{g}/\text{m}^3$). Surface concentrations of black
42 carbon (BC) (mean value $\sim 0.1 \mu\text{g}/\text{m}^3$) show peak values in the winter. The simulated values are
43 compared to surface measurements of AOD, and $PM_{2.5}$, PM_{10} , BC, organic carbon (OC) mass
44 concentrations at two regional sites in the Kyrgyz Republic (Lidar Station Teplokluchenka (LST)
45 and Bishkek). The predicted values of AOD and PM mass concentrations and their seasonal
46 cycles are fairly well captured. The carbonaceous aerosols are underpredicted in winter, and
47 analysis suggests that the winter heating emissions are underestimated in the current inventory.

48 Dust, from sources within and outside CA, is a significant component of the PM mass and drives
49 the seasonal cycles of PM and AOD. On an annual basis, the power and industrial sectors are
50 found to be the most important contributors to the anthropogenic portion of $PM_{2.5}$. Residential
51 combustion and transportation are shown to be the most important sectors for BC. Biomass
52 burning within and outside the region also contributes to elevated PM and BC concentrations.
53 The analysis of the transport pathways and the variations in particulate matter mass and

54 composition in CA demonstrate that this region is strategically located to characterize regional
55 and intercontinental transport of pollutants. Aerosols at these sites are shown to reflect dust,
56 biomass burning and anthropogenic sources from Europe, South, East and CA, and Russia
57 depending on the time period.

58 Simulations for a reference 2030 emission scenario based on pollution abatement measures
59 already committed to in current legislation show that $PM_{2.5}$ and BC concentrations in the region
60 increase, with BC growing more than $PM_{2.5}$ on a relative basis. This suggests that both the health
61 impacts and the climate warming associated with these particles may increase over the next
62 decades unless additional control measures are taken. The importance of observations in CA to
63 help characterize the changes that are rapidly taking place in the region are discussed.

64 **1. Introduction**

65 Central Asia (CA), a region of republics located between Europe and Asia, faces severe
66 environmental problems, with origins dating back to the 1960s and best symbolized by the Aral
67 Sea catastrophe (Whish-Wilson, 2002). The Aral Sea has shrunk to only about 30 percent of its
68 1960 volume and roughly half its geographical size due to diversion of water for crop cultivation
69 and other purposes. The resulting desertification of the lake-bed has resulted in extensive dust
70 storms from the region, which have impacted the surrounding agriculture, ecosystem, and the
71 population's health.

72 The 2012 Environmental Performance Index (EPI), which tracks performance of 132
73 countries across a variety of environmental and ecosystem vitality indicators, ranked CA
74 countries among the weakest performers (Kazakhstan 129, Uzbekistan 130, Turkmenistan 131,
75 Tajikistan 121, and Kyrgyzstan 101) (Emerson et al., 2012). CA and the surrounding areas are
76 developing quickly and air pollution emissions are projected to increase significantly for the next
77 several decades (Shindell et al., 2012). In recognition of the need to improve the environmental
78 conditions in the region five CA countries have formulated the Framework Convention on
79 Preservation of Environment for Sustainable Development of CA (UNEP, 2006).

80 Despite the awareness of the environmental conditions, it remains an understudied region
81 and there is a general lack of air pollution observations within CA. Furthermore the recent
82 assessment of the intercontinental transport of pollution (HTAP, 2010) has indicated that the
83 major transport pathway of pollution from Europe to Asia is via low altitude flows passing
84 through CA. The magnitude of the pollution transport from Europe to Asia is highly uncertain in
85 large part due to the lack of observations of pollutants along this pathway. To help better
86 characterize the air pollution levels and the transport pathways in the region a study was

87 undertaken between Russia, Kyrgyz Republic, and USA scientists to observe and model aerosols
88 in the region. Measurements of particulate matter (PM) mass and composition were taken at two
89 locations in the Kyrgyz Republic (Lidar Station Teplokluchenka (LST) and Bishkek) and
90 modeling analysis was performed to assess the contributions of local, regional and distant
91 sources to the PM concentrations in the region (Miller-Schulze et al., 2012, Chen et al., 2012,
92 2013).

93 In this paper we present a modeling analysis of $PM_{2.5}$, PM_{10} , ($PM_{2.5}$ refers to particles in
94 the size range of less than 2.5 μm aerodynamic diameter (AD) and PM_{10} refers to particles in the
95 size range of less than 10 μm AD), black carbon (BC) and organic carbon (OC) mass
96 concentrations and aerosol optical depth (AOD) over the time period of April 2008 to July 2009.
97 The Sulfur Transport and dEposition Model (STEM), a hemispheric chemical transport model
98 (D'Allura et al., 2011), is used to estimate spatial and temporal variations in PM in CA, and to
99 assess the contributions to PM from wind-blown dust, open biomass burning, and anthropogenic
100 sources, and different geographical source regions and source sectors (transportation, power,
101 industry and residential). The simulated values are compared to surface measurements of AOD,
102 $PM_{2.5}$, PM_{10} , BC, OC mass concentrations at the two regional sites in CA. The transport of
103 aerosols into CA is also explored through three dimensional backward trajectory analysis.
104 Transport from CA and their impacts on downwind areas are also analyzed via forward trajectory
105 analysis. Finally we present results of how the PM concentrations may change in the future using
106 emission scenarios for 2030 that reflect possible air quality and climate policies.

107

108 **2. Data and Methods**

109 2.1. Observations

110 Surface observations from two sites established in the Kyrgyz Republic to measure PM
111 concentrations and AOD in CA are used in the analysis. The locations of the Bishkek
112 (42°40'46.65"N, 74°41'38.13"E, elevation 1743 above sea level (ASL)) and LST
113 (42°27'49.38"N, 78°31'44.17"E, elevation 1921 m ASL) sites are denoted by circle and triangle
114 markers, respectively, in Fig. 1. Both sampling sites are in mountain ranges with valleys to the
115 north, with mountains that reach elevations greater than 3500 m ASL south of the Bishkek site
116 and 4600 m ASL south of the LST site, and essentially no population to the south. At each site,
117 PM_{2.5} mass was measured continuously with tapered element oscillating microbalance (TEOM)
118 instruments and PM_{2.5}, PM₁₀, BC, and OC were obtained using filter-based sampling with
119 samples collected for 24 h every other day. AOD was measured every day at 10:30 am local time
120 (LT) using Microtops-II sun-photometers (SP). A stationary three wavelength aerosol Lidar
121 measured vertical profiles of extinction and depolarization on an event basis at the LST site. The
122 Lidar vertical profiles provide information on vertical distribution of the particles, and were also
123 used to calculate AOD from the Lidar Extinction (LE) profiles and to estimate the height of the
124 planetary boundary layer (PBL) as described in Chen et al., (2013). These observations sites are
125 now part of the UNEP project ABC measurement network
126 (<http://www.rrcap.ait.asia/abc/index.cfm>). Further details of the study can be found in Miller-
127 Schulze et al., (2011). Observations from these sites were obtained for the period April 2008 to
128 July 2009 (the TEOM measurements were available from April 2008 and filter measurements
129 began from July 1, 2008).

130 In addition, the model prediction skill in simulating BC is evaluated using the BC
131 measurements from the IMPROVE (Interagency Monitoring of Protected Visual Environments)
132 surface site network
133 (<http://views.cira.colostate.edu/web/DataWizard/>)

134 The Moderate Resolution Imaging Spectroradiometer (MODIS) collection 5.1 Level 2
135 AOD products (~ 10 km horizontal resolution) at 550 nm wavelength from Terra and Aqua
136 satellites were used to compare the observed and simulated AOD. The MODIS Level 2 data were
137 used and included land and ocean AOD retrieved via the dark target algorithm (Remer et al.,
138 2005, Levy et al., 2007), and the Deep Blue AOD over land (Hsu et al., 2004, Hsu et al., 2006),
139 which can retrieve AOD over bright and desert surfaces. This is particularly relevant for the CA
140 region, which contains major dust sources in western China, South Asia, the Middle East, and
141 Africa (Ginoux et al., 2001). The MODIS Level 2 to Level 3 averaging procedure outlined in
142 Hubanks et al., (2008) was employed to interpolate the 10 km Level 2 AOD products to the 60
143 km horizontal model resolution on a daily basis. Level 2 QA flag weightings were used to reduce
144 the uncertainty associated with the MODIS retrievals. In grid cells where both the MODIS dark
145 target and Deep Blue AOD were retrieved, the mean value of the two was used.

146 **2.2. Modeling System**

147 2.2.1 Meteorological Model

148

149 The Weather Research and Forecasting (WRF) model (Skamarock et al., 2008) version
150 3.2 was used to generate the meteorological fields needed for simulating the transport patterns in
151 the STEM model (D'Allura et al., 2011). The WRF simulations for each day were initialized
152 using the meteorological boundary conditions obtained from National Centers for Environmental

153 Prediction (NCEP) Final Analysis (FNL, <http://rda.ucar.edu/datasets/ds083.2/>). A daily 24 hour
154 spin up time for WRF was used (i.e. WRF was run for 48 hours each day and the first 24 hours
155 were treated as spin up and were discarded). The STEM model simulation time period was from
156 April 2008 to July 2009.

157 2.2.2 Chemical Transport Model

158 The STEM model (Carmichael et al., 2009) was used to simulate the mass of sulfate, BC,
159 OC, other primary emitted PM_{2.5}, and other primary emitted PM₁₀ (i.e., non-carbonaceous PM
160 such as fly ash, road dust, and cement), which were simulated as a single mass component with
161 aerodynamic diameters less than or equal 2.5 μm, and between 2.5 and 10 μm (denoted as coarse
162 fraction), respectively and referred to in this paper as OPM_{2.5} and OPM₁₀, dust (fine and coarse)
163 and sea salt (fine and coarse). Nitrate and secondary organic aerosols (SOA) were not included in
164 the model for this application. The nitrate aerosol is estimated to be a minor component of the
165 PM mass in CA (Baurer et al., 2007). The importance of SOA will be discussed later in the
166 paper. The dry deposition of aerosols was modeled using the “Resistance in Series
167 Parameterization” (Wesely and Hicks, 2000) and wet deposition was calculated as a loss rate
168 based on the hourly precipitation calculated from the WRF model. Further details of the wet
169 scavenging can be found in Adhikary et al., (2007). The modeled AOD at 550 nm wavelength
170 was calculated using the simulated three dimensional aerosol distributions and species specific
171 extinction coefficients as described in Chung et al., (2010).

172 2.2.3 Modeling Domain

173 The STEM and WRF computation domains were identical, with a 60 ×60 km horizontal
174 resolution (249 ×249 horizontal grid cells) and 22 vertical layers up to 10 hPa. The domain (Fig.
175 1) covered much of the northern hemisphere in a polar stereographic projection, centered over
176 the Arctic region and extended to 35° N to include the major emission regions of North America,
177 Europe, and Asia. This modeling system has been applied to simulate aerosol distributions for
178 ARCTAS field campaign as described in D’Allura et al., (2011) and further details describing the
179 model can be found there. STEM was initialized with a one month spin up using March 2008.
180 Much of the analysis for this paper is focused on the domain denoted by the rectangle centered
181 over CA shown in Fig. 1. This domain has large gradients in topography (insert Fig. 1), which
182 significantly impact the transport patterns in the region.

183

184 2.2.4 Air Mass Trajectories

185

186 The CA observation sites are impacted by dust, anthropogenic pollution, and biomass
187 burning emissions from various source regions. To further understand the transport pathways and
188 source region influences on the PM distributions at these sites, three dimensional ten day air
189 mass trajectories (both forward and backward in time) from each site were calculated for the
190 entire time period (April 2008 – July 2009). In this trajectory analysis, we utilized the three
191 dimensional wind fields (including u, v and w components) along with the above ground level
192 (AGL) altitude simulated by the WRF meteorological model consistent with Dallura et al., 2011
193 study. These trajectories describe the general flow patterns based on wind fields alone and
194 provide useful information about the history of air mass particularly the influence of source
195 regions over which the air mass had resided before arriving at the site of interest. Note that these

196 trajectories do not account for any other atmospheric processes such as diffusion or chemical
197 evolution along its path (Kurata et al, 2004 and Guttikunda et al., 2005).

198 To understand the differences in transport patterns at the surface and aloft, and to study
199 the impact of topographic gradients in the vicinity of the sites, trajectories were initialized at
200 different altitudes (0.1 (100m), 0.3 (300m) 0.5 (500m), 1, 2, 3, and 5 km) a.g.l at the site
201 locations (i.e. latitude and longitude) daily every 3 hours for a ten day period both backward and
202 forward in time. The trajectories were terminated when they touched the ground, or went out of
203 the model domain or exceeded the ten day calculation period. The trajectories (at or below 1 km)
204 were used to characterize transport pathways impacting the surface concentrations at these sites,
205 which are discussed later in section 3.5.

206 207 **2.3. Emissions**

208 209 **2.3.1 Base emissions**

210
211 Anthropogenic emissions of BC, OC, PM_{2.5}, PM₁₀, and SO₂ were based on the ARCTAS
212 emissions described in D’Allura et al., (2011), but updated with newly available information. For
213 India and China BC, OC, and SO₂ emissions from Lu et al., (2011) were utilized, and INTEX-B
214 emissions were used for the rest of Asia (Zhang et al., 2009). For Europe, the EMEP 2008
215 (<http://www.ceip.at/webdab-emission-database/officially-reported-emission-data>) emissions were
216 used for SO₂, PM_{2.5}, and PM₁₀, and the EUCAARI 2005 inventory was used for the
217 carbonaceous particles (BC and OC) (Visschedijk et al. 2009 and Denier van der Gon et al.
218 2009). The shipping emissions came from the IIASA base year 2005 inventory (UNEP and
219 WMO, 2011). Mass conservative regrinding tools including MTXCALC and MTXCPL from

220 the IOAPI m3tools suite (<http://www.baronams.com/products/ioapi/AA.html#tools>) were used to
221 interpolate the input raw emissions described above on to the model grid.

222 Anthropogenic emissions for SO₂, BC and OC were available by major economic sectors;
223 i.e., transportation, residential, industry, and power. The industry and power sectors were treated
224 as small and large point sources, respectively, and emitted into the first 6 model levels (lowest 2
225 km). The residential and transportation emissions were treated as near surface area sources and
226 partitioned into the first two model levels from surface to ~ 100m (i.e. AGL altitude of level 2)
227 with a 90 – 10 percent split. Monthly emission allocation factors were applied over India and
228 China for the economic sectors from Lu et al., (2011). The rest of the domain (i.e. excluding
229 India and China) used same emission rates for all months due to unavailability of monthly
230 emission allocation factors.

231 The Fire Inventory from NCAR (FINN v1) was used for BC, OC, CO, SO₂, PM_{2.5} and
232 PM₁₀ biomass burning emissions from forest, grassland and crop residual fires. The FINN
233 database, which is based on MODIS fire detection as thermal anomalies, provides global
234 coverage of fire emissions at a spatial resolution of ~ 1km on a daily timescale (Wiedinmyer et
235 al., 2011). The WRF-Chem fire utility (<http://bai.acd.ucar.edu/Data/fire/>) was employed to
236 interpolate the speciated FINN emissions to the WRF model grid. The gridded two-dimensional
237 FINN emissions were used as input to the WRF-Chem (Grell et al., 2005) plume rise model
238 (Grell et al., 2011), which implements the Freitas et al., (2007) and Freitas et al., (2010)
239 algorithm to compute injection heights and to calculate the vertical distribution of fire emissions
240 at an hourly time step, which were further utilized as input to STEM model simulations.

241 Sea salt and dust emissions were calculated using the WRF meteorological fields based
242 on the methods described in Gong, (2003) and Uno et al., (2004), respectively. The dust
243 emissions were further constrained with snow cover (SNOWC variable from WRF output) and
244 only grid cells with snow cover < 1% were used for dust emission calculations.

245 Fig. 2 shows the annual gridded anthropogenic SO₂ and BC, dust, and biomass burning
246 PM_{2.5} emissions in Gg per grid in and around CA. Large BC emission hotspots can be seen over
247 the Indo-Gangetic plain and eastern China. Significant BC emissions are also seen over Europe,
248 but are relatively lower in intensity than the Asian sources. The SO₂ emissions show Eastern
249 China as the largest source region followed by regions of South Asia, Europe, and Russia. The
250 major natural dust emission sources (Fig. 2c) include Africa, the Middle East, CA, Western India
251 boundaries, and Western China. The major sources of biomass burning are Eastern Europe,
252 portions of Siberian (between 40 – 60° N), Southeast Asia, Southern China and India (Fig. 2d).

253 Dust emissions have a strong seasonal cycle. The major dust sources in the region (Fig.
254 1) are located to the east, west and south of the observation sites and include the cool winter
255 deserts around the Aral and Caspian seas and those in western China and northern Pakistan as
256 well as the sub-tropical deserts in western India, around the Persian Gulf and northern Africa.
257 The emissions from the cool winter deserts occur when the surfaces are free of snow cover (from
258 March through October). Emissions from the sub-tropical deserts can occur throughout the year.

259 The open biomass burning emissions that impact CA also have a strong seasonality with
260 minimum impact in winter (Supplemental Materials Fig. S1). Fires typically begin in the spring
261 in Siberia along 50° N latitude and in northern India and South East Asia and in summer the high
262 latitude burning shifts to the west. In October the fire activity decreases and remains low until

263 spring, with the most active fire regions associated with agricultural burning in northern India
264 and southeast China.

265 **2.3.2 Future Emissions Scenarios**

266 In addition to the base emissions, a series of simulations were analyzed using emission
267 scenarios for 2030. These scenarios were developed for the WMO/UNEP report that looked at
268 short lived climate pollutants as described in Shindell et al., (2012) and Anenberg et al., (2012).
269 The reference scenario for 2030 was based on the implementation of control measures currently
270 approved in the various regions and assumed their perfect implementation. The 2030 reference
271 scenarios were developed from a reference global emissions inventory with a 2005 reference
272 year, and assumed significant growth in fossil fuel use relative to 2005, leading to increases in
273 estimated CO₂ emissions (45%). Abatement measures prescribed in current legislation were
274 projected to lead to reductions in air pollutant emissions, which varied by pollutant and region.
275 In the 2030 reference scenario, total primary PM_{2.5} emissions remain approximately constant,
276 while BC and OC decline by a few percent. However, in the study domain emission changes
277 varied widely. BC emissions increased by 10 – 100% in CA, South and Southeast Asia and in
278 western China, and decreased in East Asia and Europe. The PM_{2.5} emissions showed similar
279 regional changes but grew at smaller rates (10 – 40%). SO₂ emissions generally increased
280 throughout the region by 10 – 20%. Spatial maps of emission changes for the 2030 reference
281 scenario are presented in Figs. S2b, S3b, and S4b.

282 A series of emission control scenarios for 2030 were developed to evaluate the impact of
283 additional abatement measures designed to reduce the levels of short lived climate pollutants
284 (e.g., BC). The BC measures in the scenarios included two different sets of assumptions (low and

285 lowest). The first focused on reductions from incomplete combustion sources. These included
286 implementation of Euro 6 equivalent vehicle emission standards (requiring installation of diesel
287 particulate filters) and improving traditional biomass cook stoves in developing countries
288 (assuming 25% decrease in BC and 80 – 90% decreases in OC, CO, non-methane volatile
289 organic compounds(NMVOC), methane, and direct PM_{2.5}, relative to emissions from traditional
290 stoves). Under this scenario BC and PM_{2.5} emissions in the study region are projected to decrease
291 throughout most of the domain, with SO₂ emissions showing almost no change (see Figs. S2c,
292 S3c, and S4c).

293 The lowest option assumed the additional elimination of high-emitting vehicles, biomass
294 cook stoves (in developing countries), and agricultural waste burning. These BC measures in the
295 lowest scenario reduced global anthropogenic BC emissions by 75%. Measures targeting BC
296 also substantially reduced total primary PM_{2.5} (-50%), OC (-79%), NO_x (-27%), and CO (-44%).
297 These BC measures have little impact on SO₂ emissions. Projected emissions of BC and OC
298 under these scenarios are reduced most in Asia, followed by Africa. North America, and Europe.

299 These measures were also combined with a scenario designed to stabilize greenhouse
300 gases at 450 ppm of CO₂ equivalent (lowest+450ppm scenario), consistent with a global average
301 temperature increase of ~2° C. These CO₂ measures reduced SO₂ (-30%) (Fig. S4d) and NO_x (-
302 20%), but had little further impact on BC (~5% decline, Fig. S2d) since the major sources of CO₂
303 differ from those of BC. PM_{2.5} emissions were substantially further reduced under this scenario
304 (Fig. S3d).

305 **2.4. Simulations Analyzed**

306 The CA region is strategically located and aerosols at these sites are shown to reflect
307 impact of varied dust (including CA, Western China, Africa and Middle East), biomass burning
308 (including Europe, Siberia, South Asia and North America) and anthropogenic sources
309 (including Europe, South, East and Central Asia, and Russia) depending on the time period. So
310 we choose different regions for the anthropogenic, dust and biomass burning in order to capture
311 the impact and the associated seasonality of these main regions on the regional distribution of
312 aerosols in this region. We have more anthropogenic regions to better understand how regional
313 changes in emissions may impact CA PM levels.

314 Several simulations were analyzed for this paper. The *base* simulation included all
315 sources and used the meteorology from the WRF model for the period April 2008 – July 2009.
316 To investigate the contributions from specific source sectors, additional simulations were
317 performed where emissions from one sector were set to zero everywhere. The contribution from
318 each sector was calculated as the difference between the base simulation and the simulation with
319 emissions from that particular sector set to zero. This was repeated for each sector and for
320 biomass burning. Additional simulations were performed to assess the source contribution from
321 specific regions to the particle levels in CA. The specific regions used are shown in Fig.1. In
322 these simulations all anthropogenic emissions were set to zero in that region. In a similar manner
323 regional dust and fire sources were also studied and the source regions are also shown in Fig.1.
324 Finally, simulations were performed using the *reference* 2005 and 2030 emissions and the *low*
325 and *lowest + 450 CO₂* 2030 scenarios (described above). For these runs, the meteorology, open
326 biomass burning, and dust emissions were the same as in the base run (i.e., 2008/2009).

327 **3. Results and Discussion**

328 We have evaluated this model framework in other regions outside CA including arctic
329 region and continental US previously, which are summarized below. The domain configuration
330 and settings of the WRF/STEM modeling system used in this study have been applied to provide
331 meteorology and air quality forecasting during the ARCTAS field campaign in 2008 (Dallura et.
332 al., 2011) as mentioned earlier in sections 2.2.3 and 2.3.1 respectively. The study by Dallura et
333 al., used WRF v2.2 and pre-emission ARCTAS emissions data
334 (http://mic.greenresource.cn/arctas_premission), real time biomass burning emissions from the
335 RAQMS modeling group (<http://raqms-ops.ssec.wisc.edu/>) and evaluated the performance of the
336 WRF-STEM modeling framework (used in this study) through the case study of the ARCTAS
337 mission DC-8 flight conducted on July 9 2008. The WRF model compared well with observed
338 meteorological variables (including temperature, pressure, wind speed and wind direction) along
339 the flight and correctly simulated the various meteorological processes (i.e. cyclonic circulation,
340 low pressure system, anticyclones and geostrophic wind flows) that facilitate transport of
341 pollutants into the Arctic region. This study also compared CO along the flight and found that
342 the simulated values were able to capture the magnitude and temporal variability seen in
343 observed values. The study also found that the fires from North Asia and anthropogenic CO from
344 China were the major sources contributing to observed CO levels along the flight suggesting that
345 the midlatitude pollution and summertime forest fires/biomass burning transport events were
346 well represented in this modeling system.

347 Huang et al, 2012 used a subset of this domain (covering the region of continental North
348 America) to simulate summertime sectoral and regional contributions to BC over continental US
349 using the WRF/STEM modeling framework. Note that the Huang et al., 2012 study used the
350 same WRF meteorology, ARCTAS emissions and RAQMS biomass burning emissions used in

351 the Dallura et al., 2011 study, but used the full-chemistry version of the STEM model. The
352 comparison of the simulated aerosol BC from the STEM tracer model with corresponding BC
353 values from the full chemistry version of the STEM model showed that the simulated tracer BC
354 was able to capture trend and the same relative variability seen in the full chemistry predictions.
355 Huang et al., 2012 evaluated the model performance aloft and at surface using measurements
356 from ARCTAS mission DC8 flights conducted on June 20 and 22 and 24 that sampled over
357 California and IMPROVE surface site network. Huang et al., 2012 found that the predicted BC
358 values captured many of the vertical features seen in the flight observations with a tendency to
359 over predict surface BC and > 4km. The comparison of predicted BC with observed values from
360 the IMPROVE network showed that the model was able to capture the gradients in BC values
361 with high concentrations in western and eastern NA regions with slight positive and negative
362 biases over the mountain regions and the eastern US/California.

363 These studies indicate that the simulated transport patterns are able to capture the main
364 important features of the hemispheric flows at the scale hemispheric flows impacting Central
365 Asia, North America and the Arctic region, at the scale discussed. The prediction of aerosol mass
366 and composition at the hemispheric scales are able to capture important aspects of horizontal
367 gradients and variability, but has considerably higher uncertainties associated with emission
368 estimates (in particular forest fires/biomass burning and natural dust emissions) and wet removal
369 processes (Bates et al., 2006).

370

371 **3.1 Comparison with surface BC observations from IMPROVE network**

372 We evaluated the simulated BC values with IMPROVE BC observations for the simulation
373 time period (i.e. April 2008 – July 2009) used in this study. The IMPROVE BC analysis is
374 limited to 27 sites on the US west coast (i.e. west of 120 W) to be consistent with the focus of
375 this paper (i.e., long range transport of pollutants on a hemispheric scale). The mean observed
376 and modeled BC for the West Coast sites are ~ 0.16 and $0.19 \mu\text{g m}^{-3}$ ($n = 3759$ points) with
377 mean bias and RMSE of $0.03 \mu\text{g m}^{-3}$ and $\sim 32\%$ respectively. The mean simulated/observed BC
378 at surface sites is ~ 1.2 , which compares well with the corresponding ratio of 1.6 reported in the
379 global model performance over North America region by Koch et al., 2009. The detailed analysis
380 of the IMPROVE BC sites and associated seasonality will be the addressed in a future paper. The
381 rest of this section will focus on discussing the regional aerosol distributions in the CA region.

382 **3.2. CA Regional Perspective**

383 CA is a region with high aerosol loadings as shown in the mean MODIS retrieved AOD
384 at 550 nm for the time period of study (April 2008 – July 2009) (Fig. 3). AOD (period mean)
385 throughout CA ($\sim 45\text{-}90^\circ$ E, $35\text{-}50^\circ$ N) are greater than 0.25, with the highest regional values
386 around the desert areas near the Caspian and the Aral seas. There are also high values (>0.6)
387 along CA's eastern border, which reflect the deserts and rapidly developing cities in western
388 China, and to the south over Pakistan and northern India.

389 The predicted period mean AOD spatial distribution shown in Fig. 4d captures the main
390 observed features. The period-mean predicted surface concentrations of $\text{PM}_{2.5}$, BC, and total dust
391 (fine and coarse) are also plotted. The period mean $\text{PM}_{2.5}$ concentrations in CA (10 to $35 \mu\text{g}/\text{m}^3$)
392 have a similar geographical distribution as AOD. Dust is the major component of predicted PM_{10}
393 in CA and concentrations are high ($25\text{-}100 \mu\text{g}/\text{m}^3$). The BC levels in CA are typically less than

394 0.3 $\mu\text{g}/\text{m}^3$ and its spatial pattern reflects contributions from both anthropogenic and biomass
395 burning sources.

396 **3.3 Comparison with surface observations in CA**

397 The surface observations at the two CA sites provide the opportunity for the first time to
398 evaluate the performance of chemical transport models in estimating the distribution of aerosols
399 in CA and to assess the emission estimates in the region. A comparison of the predicted and
400 observed meteorology is presented in Fig. 5, where the distributions of key meteorological
401 parameters for the entire measurement period are shown as box-plots. The model accurately
402 predicted the magnitude and variability in temperature and relative humidity. For example the
403 model mean value of temperature and relative humidity are 279.3K and 61.6% in comparison to
404 the observed values of 280.3K and 59.2% at the LST site. The model wind speeds were biased
405 high by about 30% (mostly in winter, see section 3.4) and the direction had a southwest bias.
406 These biases are due in part to the 60 km model grid size, which is too coarse to capture the steep
407 gradients in topography in and around the observation sites, and to the site placement in small N-
408 S oriented valleys. More details regarding the evaluation of the modeled meteorology can be
409 found in the Supplemental Materials, Table S1.

410 The observed and modeled distributions of AOD and PM are compared in Fig. 6. The
411 AOD observations based on the LE on average are ~50% larger than those from the SP. Modeled
412 AOD on average are ~20-30% higher when compared to SP at the Bishkek and LST sites and ~1
413 % lower when compared to the LE values. The variability in the predictions is slightly under-
414 estimated. $\text{PM}_{2.5}$ is over predicted (~50%) and the spread is accurately captured, while PM_{10} is
415 over predicted by ~70%. This leads to an underestimation of the $\text{PM}_{2.5}/\text{PM}_{10}$ (0.4 predicted

416 versus 0.5 observed) and also helps account for the overestimation in modeled AOD (by ~20-
417 30%).

418 Chemical analysis of the filter and soil samples in the CA dust regions have been used to
419 estimate the dust contribution to measured PM at the two sites and to help identify source regions
420 of importance (Park et al., 2014). The emission regions within CA, including around the Aral
421 Sea, and western China were identified as the most important dust sources, which is consistent
422 with the regions identified in the simulations. Dust was estimated to comprise between 5-40% of
423 PM_{2.5} mass at the LST site and to vary by season (minimum values in winter). The observation-
424 based estimates of dust percentage contribution suggest that modeled dust is over predicted by
425 ~2 times. Thus it appears that dust is a main reason for the over prediction of PM_{2.5} and PM₁₀,
426 and that dust emission models need to be refined for CA applications.

427 The overestimation in PM mass at the surface could also be impacted by errors in the
428 modeled PBL heights. The PBL height as determined by the Lidar aerosol profiles varies
429 seasonally and is highest in the summer (from 2-4 km AGL) and lowest in the winter (Nov-Feb,
430 0.5-1.5 km AGL) (Fig. S5). The predicted PBL heights show a similar seasonal cycle with a
431 tendency to under-predict the heights in all seasons as indicated by the comparison of the
432 distributions of the observed and predicted values (Fig. 5), and this occurs in all seasons (Fig
433 S5). The lower PBL height in the model contributes a systematic high bias in surface
434 concentrations driven by near surface emissions. Further statistical details of the model-
435 observation comparison can be found in the supplemental materials (Tables SM2 & 3). The
436 seasonal variability in the observations is discussed in further detail later (section 3.4).

437 **3.4 Source Contributions to PM_{2.5}**

438 Model simulations were performed to identify the component, source region and
439 emission sector contributions to $PM_{2.5}$ mass. Period means for the spatial average over the entire
440 CA region (see Fig. 1) and for the grid cells for the Bishkek and LST observation locations are
441 presented in Fig.7, and their comparison provides insights into the spatial variability of PM and
442 its sources within CA, and how representative the observation sites are at characterizing CA PM.
443 The component contribution to AOD at the sites and for the CA average are similar, with the
444 major contributions coming from fine dust, sulfate, and OC. Spatial maps of mean percent
445 contributions of the various components (i.e., BC, OC, sulfate, OPM, dust and sea salt) to AOD
446 and $PM_{2.5}$ mass are presented in Figs. S6 & S7, respectively. Coarse particles contribute ~10% to
447 mean AOD. Dust accounts for >60% of the calculated $PM_{2.5}$ mass at the observation sites and for
448 the CA region. The dust source regions (see Fig. 1) contributing to $PM_{2.5}$ vary within CA. Dust
449 from the CA source regions has the largest influence on the region mean dust- $PM_{2.5}$ mass. At the
450 LST site, which is located in the far east of CA, western China dust sources have their largest
451 influence (~40%). African and Middle East source regions have their largest influence on the
452 Bishkek site (20 and 15%, respectively), and collectively contribute ~25% to regional CA dust
453 $PM_{2.5}$.

454 The source region contributions to the non-dust $PM_{2.5}$ are very similar for the Bishkek
455 and LST sites, with CA sources making the largest contribution (~50%) followed by Europe
456 (~20%), the Middle East (~15%), and biomass burning (~15% from all sources). For the entire
457 CA region the European source contribution is as large as the CA sources (~30% each), with
458 larger contributions from biomass burning and Russia sources and smaller contributions from
459 Middle East emissions than at the observation sites. The significant contribution from Europe
460 sources reflects their large anthropogenic emissions and the general westerly transport patterns.

461 On average the impact from South Asia sources are small. North America sources contribute
462 between 3 to 7% to $PM_{2.5}$ in CA. Of the biomass burning contribution to $PM_{2.5}$, the Siberian and
463 European fires (see Fig. 1 for fire regions) contribute 63 and 25%, respectively, with
464 contributions from South/Southeast Asia and North America fires each contributing ~5%. The
465 power and industrial sectors are identified by the simulations as the largest contributors (~40%
466 each) to non-dust $PM_{2.5}$ mass in CA.

467

468 **3.5. Seasonal Variations in AOD and PM at the Observation Sites**

469 AOD has a seasonal cycle with the lowest values in winter and highest values in spring
470 and summer as shown in Fig. 8 by the AOD observations at the LST site from both the SP and
471 the LE profiles. A similar seasonal cycle was observed at the Bishkek site (not shown) and in
472 the MODIS AOD retrievals (Fig. S8). The modeled AOD captures this seasonal variation, with a
473 tendency to over predict the values during the periods with the lowest observed AOD.

474 The seasonal cycles in $PM_{2.5}$ (Fig. 9) and PM_{10} are similar to those for AOD, with
475 minimum values in October – February. At the LST site $PM_{2.5}$ from both the filter based and the
476 non-volatile TEOM measurements are plotted. Both the observations and the model find a strong
477 similarity in the time series at the two sites.

478 There is also a clear seasonality in the surface meteorology in the region as shown by the
479 time series in surface temperature and relative humidity at the two sites (Fig. 10). There are
480 distinct temperature minima in the winter and relative humidity minima in the summer. However

481 there is not a clear seasonality in wind speed and direction, and the winds are generally from the
482 south and less than 4m/s throughout the year at the LST site (not shown).

483 The source region and component contributions exhibit seasonal variability as shown by
484 the modeled contributions to $PM_{2.5}$ mass in Fig. 11. Dust is found to be the main driver of the
485 seasonal cycle of $PM_{2.5}$. The dust contribution to $PM_{2.5}$ is peak in spring and minimum in winter
486 (<20%). During this time period the transport of air masses to the sites are from the west and the
487 southwest. When the transport is from the east then dust sources from western China can impact
488 the stations. This transport pattern occurs episodically throughout the year, with contributions
489 from western China sources as large as 20 to 50%. The dust seasonal cycle is in turn influenced
490 by the seasonal variations in meteorology that drives the dust emissions and transport. The
491 seasonal changes in the dust source regions can be seen in the seasonal spatial maps of AOD
492 (Fig. S8). Throughout the domain, AOD in the dust regions are highest in March – October and
493 lowest in winter (Fig. S8) as the nearby dessert regions are snow covered.

494 Biomass burning also adds to the seasonal cycle, and its contribution is minimum in the
495 winter. South Asia sources can impact the sites in the winter time. The periods when North
496 America sources impact the site are associated with strong transport events across the Atlantic
497 and subsequent subsidence towards the surface associated with high pressure systems as they
498 move towards CA. The transport pathways are discussed in more detail in Sect. 3.7.

499 **3.6 Source Contributions to BC**

500 Because of its dual role as an air pollutant and as a climate warming agent there is special
501 interest in understanding the regional and sector contributions to BC (Ramanathan and

502 Carmichael, et al., 2008). BC comprises on average only about 1-2% of PM_{2.5} mass in CA. The
503 period mean predicted BC surface concentrations are ~0.1 µg/m³ at the two observation sites and
504 0.15 µg/m³ for the CA regional average. As shown in Fig. 7, European emissions contribute
505 ~50% to the mean BC concentrations in CA, while Middle-eastern and biomass burning sources
506 each contribute ~15-20%. Residential and transport are the most important sectors each
507 contributing ~30% to BC in CA, followed by industry (~20%), and with power the least
508 important. This is in contrast to the sector contributions to non-dust PM_{2.5} mass, where power
509 and industry are the most important sectors. On average biomass burning contributes ~10% to
510 BC mass, with Siberian and European fires accounting for 61% and 33%, respectively. The
511 source contributions to OC are shown in Fig. S9.

512 There is also large seasonal variability in BC concentrations and source sector/region
513 contributions (Fig. 12). BC surface concentrations show the highest values in fall/winter (as do
514 the observations), when there is maximum contribution from the residential sector, reflecting the
515 wide-spread use of biofuels and coal for heating in the region. The source region contributions
516 vary by season, with maximum contributions from Europe and China. South Asia sources
517 contribute in the winter. Biomass burning also is an important source of BC and plays an
518 important role in influencing daily and seasonal variability in BC concentrations.

519 Predicted BC captures the seasonality and the magnitude of the spring and summer
520 values as observed, but concentrations are biased low in the fall/winter. Median BC
521 concentrations (and variability) are underestimated by a factor of 2 at both observation sites (Fig.
522 6 and Tables S2&3)). The high wind speed bias in winter (~ factor of 2), should result in too
523 rapid dispersion and could contribute to the negative bias, but the negative bias in the PBL

524 heights should lead to higher predicted concentrations. Thus this negative bias is likely related to
525 emissions (an indication of an underestimation of the heating fuel use).

526 The OC concentrations follow a similar seasonal cycle as BC and are also under
527 predicted (Fig. 6 and Tables S2 & 3)). Furthermore the OC/BC ratio is under predicted by a
528 factor of ~3 (Fig. 6). The observed OC/BC ratio follows a seasonal cycle with values >15 in
529 summer and ~5 in September through April. Part of this under prediction in OC and the OC/BC
530 ratio is due to the fact that SOA is not estimated in the model. However a source contribution of
531 OC using the filter data and chemical mass balance (CMB) approach found that SOA sources
532 were very low in winter and only ~ 20% in summer (Miller-Schulze et al., 2011). Thus SOA
533 cannot account for the model under prediction of winter values. There appears to be an
534 underestimation of regional OC primary emissions. SOA can however help account for the large
535 values of OC/BC observed in the summer and not predicted.

536 Biomass burning emissions cannot account for the underestimation in winter BC and
537 OC. The largest impact of fires at the observation sites is in the late summer, when the fires are
538 concentrated in western Russia and the wind direction is such that the smoke is transported into
539 CA. Fires from South Asia can impact the sites associated with the fires and high pollution levels
540 in northern India and with winds from the south, which can occur in late fall, but not frequently.

541 The fact that BC and OC are systematically under predicted in the winter suggests that
542 local/regional emissions during the heating season may be underestimated. This is supported by
543 the results of the CMB analysis of OC discussed above that found the contribution from biofuel
544 combustion increased 2-3 times in the fall and winter periods. The uncertainty in emissions can

545 also be partly caused by the lack of seasonal emissions over this region as described earlier in
546 section 2.

547

548 **3.7 Vertical Distributions**

549 Figure 13 shows the predicted weekly averaged vertical distributions of PM_{2.5}, dust, and
550 BC for the entire simulation period at the LST site. These plots show more clearly that much of
551 the variability in the PM loadings is associated with dust and biomass burning episodes (as
552 represented by the enhancements in BC). Typically the high PM episodes show elevated PM
553 mass that extend from the surface to 2 to 4 km. The vertical extents show a seasonality
554 associated with seasonal variations in the PBL heights. These vertical distributions indicate that
555 much of the transport of aerosols in CA occurs via low altitude pathways. In some cases there are
556 large amounts of dust and biomass burning aerosol in the 3-6 km altitude range that are
557 decoupled from the surface (e.g., dust in early May 2009), reflecting that some aerosols are lifted
558 out of the boundary layer and are transported at high altitude over CA, enhancing AOD but not
559 contributing to ground-level mass concentrations at the observation sites. These vertical features
560 are confirmed by the aerosol extinction profiles observed at the LST site as discussed in Chen et
561 al., (2012 b). The variation in weekly averaged AOD can be significant (Fig. 13 bottom panel)
562 and is driven by variations in dust and biomass burning emissions.

563

564 **3.8 Transport Pathways**

565 The three dimensional ten day air mass trajectories (described in section 2.2) were utilized to
566 further understand the transport pathways of air masses entering into and exiting out of the CA
567 region and its subsequent impact of source regions on the aerosol distributions at the CA sites.

568

569 3.7.1 Transport into CA

570 The air mass transport into CA is discussed through back trajectories associated with the
571 five events labeled on Fig. 13. These five events represent transport episodes with elevated
572 surface PM_{2.5} (averaged over the three hour time window consistent with trajectory time step)
573 with varying contributions from biomass burning, anthropogenic pollution, and dust sources. In
574 each trajectory figure (Figs. 14 and 15), the regions with active dust (blue diamond hatches) and
575 biomass burning emissions (green square hatches) for the event time period and prior ten days
576 are identified and MODIS AOD (values printed in black) overlaid. The trajectories are color
577 coded by region to distinguish the source impacts. The regions include: Africa (blue), Middle
578 East (green), CA (yellow), North Asia biomass (> 50° N, black), Europe (brown), China (red)
579 and South Asia (orange).

580 Figure 14 shows the first two events for August 2008. The first event in early August
581 (Fig. 13, event labeled 1) is a high dust event associated with trajectories from the west passing
582 over the dust regions of the Aral Sea (~45N, 55E) and eastern trajectories passing over the
583 Taklimakan region of western China (90-100E, 40N). These were both regions with active dust
584 emissions as indicated by the elevated MODIS AOD values. Thus the PM increases during this
585 event were due largely to dust emitted from CA and western China deserts. The second event in

586 the latter half of August is characterized by high levels of BC without dust. During this episode
587 the transport to the site was under the influence of a high pressure system located to the
588 northwest and air masses were transported over the active fire region in western Russia.

589 Figure 15 shows winter and spring events. The November episode (event 3) is a period
590 with elevated BC and PM_{2.5} from pollution sources from South Asia (including some fires) and
591 western China and low fire and dust emission activity. The January episode (event 4) is a period
592 of elevated BC with air masses coming from Europe, indicating the influence of anthropogenic
593 pollution coming from this industrialized region, and from CA sources. Dust emissions from CA
594 and Africa were low during this period. The final illustrative episode is for April 2009 (event 5),
595 a period with both elevated levels of dust from western China, CA and Africa and BC from both
596 fire and anthropogenic pollution from Europe, CA and Russia sources.

597 These examples provide insights into the source region contributions to PM mass in CA
598 as presented in Figs. 11 & 12). CA is an ideal location to observe a variety of source regions as it
599 is at the crossroad of transport patterns with air masses impacted from dust, anthropogenic
600 activity and biomass burning from different geographical regions.

601 3.7.2 Long range transport of CA sources

602 The transport pathways out of CA were also evaluated by calculating forward trajectories
603 from the observation sites. Selected forward trajectories initialized at or below 1 km are used to
604 represent the transport of boundary layer PM from CA and these are shown for summer, winter
605 and spring periods in Fig. 16. In these plots the MODIS AOD, dust, and fire emissions plotted
606 for each event represent values averaged over the subsequent ten days and trajectories were

607 stopped if they impacted the surface. During the summer, outflow from CA is towards the north
608 in association with the summer monsoon system. Figure 16a shows the subset of forward
609 trajectories that reside for at least 3 days over the region 48 - 65° N during June 2008.
610 Trajectories typically pass over Russia and reach into the Arctic and also can be caught in
611 westerly storm tracks and reach the higher latitudes of the northern hemisphere. During the
612 winter, air mass transport out of CA is associated with the winter monsoon system and the
613 transport pathway is over Mongolia and then over eastern China as seen in Fig. 16b. In this
614 figure, forward trajectories that pass over the region west of 130° E during late December 2008
615 are shown. Figure 16c illustrates transpacific transport of CA air masses. Plotted are the forward
616 trajectories that stay within the 30 – 50° N region for at least 3 days during the month of April
617 2009. During the spring transport from CA is dominated by strong westerly flows and air masses
618 are transported over China, Korea, and Japan and then across the Pacific, reaching North
619 America in 7 – 10 days.

620 PM arising from dust and anthropogenic emissions from CA impact the entire northern
621 hemisphere as illustrated in the hemispheric maps of seasonal average surface dust
622 concentrations due to CA emissions only (Fig. 17). The predominant westerly flows in all
623 seasons in the northern hemisphere result in the bulk of the CA emissions being transported to
624 the west. The contribution of CA sources to surface PM concentrations of 0.35 $\mu\text{g}/\text{m}^3$ or greater
625 covers large portions of the northern hemisphere, including the Arctic, all of Asia, much of
626 Europe, and portions of the continental US.

627 There are episodic and seasonal components to the intercontinental transport as shown in
628 the time series of the vertical profiles of $\text{PM}_{2.5}$ at Mt. Bachelor, Oregon (43.97N, 121.69W,

629 2700m agl) (Fig. 18). The bulk of the CA particle transport takes place in the free troposphere
630 and impacts surface concentrations in the US as the boundary layer grows and entrains “plumes”
631 aloft. This occurs most frequently in spring, summer and fall. The episodic contributions of CA
632 sources to surface concentrations can exceed $1.5\mu\text{g}/\text{m}^3$. In the fall, there is also strong transport
633 of dust from CA across Europe and out into the Atlantic.

634

635 **3.9 Future Scenarios**

636 How might PM levels change in CA over the next few decades? To address this question,
637 simulations were repeated for various emission scenarios developed and used in the
638 WMO/UNEP assessment on short-lived climate pollutants (Shindell et al., 2012) as described in
639 Sect. 2. Dust and biomass burning emissions and meteorology were the same as those used in the
640 2008/2009 simulations. The period mean changes in surface BC and $\text{PM}_{2.5}$ concentrations in
641 2030 for the reference scenario are shown in Fig. 19a, d, respectively. This scenario reflects all
642 present agreed policies affecting emissions and assumes that they are fully implemented. Under
643 this scenario $\text{PM}_{2.5}$ increases significantly in South Asia and western China (>50%) and in parts
644 of CA, including the area where the sampling sites are located. $\text{PM}_{2.5}$ decreases in Western
645 Europe and Eastern China (< 10%). BC surface concentrations show a similar pattern to $\text{PM}_{2.5}$,
646 although covering larger portions of CA with relatively larger increases in BC than in $\text{PM}_{2.5}$.
647 These results suggest that health impacts and climate warming due to BC and $\text{PM}_{2.5}$ may increase
648 in coming decades unless additional emission control measures are implemented.

649 Results for two other scenarios are also presented in Fig. 19. One scenario specifically
650 targets BC emission reductions in recognition that BC is also a major contributor to atmospheric
651 warming (Ramanathan and Carmichael, 2008). These additional measures significantly reduce
652 2030 BC concentrations by greater than 35% throughout most of the domain, with only a few
653 regions (e.g., Myanmar and eastern Afghanistan) showing increases in BC relative to 2005
654 levels. This scenario assumes that all BC emission reduction measures are perfectly implemented
655 and 100% effective. BC measures also impact emissions of co-emitted pollutants (e.g., OC and
656 SO₂). PM_{2.5} concentrations under this scenario (Fig. 19e) are reduced, but by much smaller
657 amounts, and concentrations still increase relative to 2005 over large regions of South Asia and
658 western China, and parts of CA. These results suggest that health impacts in these regions may
659 increase due to the PM_{2.5} increases whereas positive radiative forcing and health effects due to
660 BC may decrease. When the BC measures are used along with greenhouse gas measures aimed at
661 keeping CO₂ levels below 450 ppm, the PM_{2.5} levels in South Asia are lower than 2005 levels
662 (Fig. 19f), with few exceptions (one being Myanmar region). This is due to the large decreases in
663 SO₂ and NO_x emissions under this scenario, resulting in significant reductions in particulate
664 nitrate and sulfate (e.g., a ~30% increase in particulate sulfate in CA).

665 To get a regional perspective of how the future emission changes would specifically
666 impact the CA region (See Fig. 1 for the CA region definition used in this study), we have
667 summarized the changes in emissions and the corresponding concentrations in Table 1. The
668 reference 2030 emissions scenario reports an increase in emissions of BC, SO₂ and PM_{2.5} over
669 Central Asia by ~ 22, 17 and 14 % respectively w.r.t to base 2005 levels. However, the
670 corresponding BC, SO₄ and anthropogenic portion of PM_{2.5} decrease by ~ 5, 12 and 5 %
671 respectively. This suggest that on average the concentration levels go down even though CA

672 emissions increase due to long range transport of pollutants into CA region from the surrounding
673 regions, but locations within CA still increase when dominated by local sources. The Low GWP
674 emission scenario predicts decrease in BC and PM_{2.5} emissions by 31% and 10% respectively
675 with the corresponding decrease in concentrations by ~ 37% and 10 % respectively, while SO₂
676 emissions remained same as the reference 2030 scenario. The lowest + 450 ppm scenario shows
677 a consistent decreasing trend in emissions and concentration of all the species. This analysis
678 suggests that the impact of the changes in major source region emissions and their subsequent
679 transport to Central Asia will play a major role in determining the future aerosol levels in CA.

680 **4. Summary**

681 AOD in CA during the period April 2008 through July 2009 averaged ~0.3 and displayed
682 a seasonal cycle with the lowest values in the winter and highest values in spring to mid-summer
683 with observed values of AOD > 0.6 and even > 0.8. Surface PM_{2.5} measured at two sites in
684 eastern CA averaged ~10 µg/m³ but with large variability (hourly values from 2 - 90 µg/m³).
685 Surface concentrations of PM also showed a seasonal cycle with peak values and largest
686 variability in the spring/summer, and lowest values and variability in the winter. BC at these sites
687 averaged ~0.1 µg/m³ with peak values (~ 1 µg/m³) in the winter.

688 The seasonal cycles and source sector and source region contributions to PM in CA were
689 analyzed using the STEM chemical transport model. Dust was the largest component of the
690 PM_{2.5} and PM₁₀ mass in the region in all seasons except winter, whereas sulfate was the largest
691 anthropogenic component of the PM_{2.5} mass. Dust was also found to be the major driver of the
692 seasonal cycles of AOD and PM concentrations. On an annual basis the power and industrial
693 sectors were the most important contributors to PM_{2.5}, while residential and transportation were

694 the most important sectors for BC. Open biomass burning within and outside the region also
695 contributed to elevated PM and BC concentrations and to the temporal variability.

696 The model simulations showed a systematic over prediction of PM mass. This is most
697 likely due in large part to the over prediction in dust. Carbonaceous PM was underpredicted and
698 it is speculated that the winter emissions associated with residential heating may be
699 underestimated in the current emissions inventory. The predicted wind speeds were biased high
700 (by ~30%) and the direction had a southwest bias. The high bias in wind speeds may also
701 contribute to the over-prediction in PM_{10} , as dust emissions depend strongly on wind speed.
702 Efforts to improve the dust emissions and to improve the wind speed and direction predictions
703 using a finer model resolution are planned. Additional efforts are needed to improve the
704 anthropogenic emissions estimates for CA.

705 Currently there are few measurements in CA that can be used to quantify the
706 intercontinental transport of pollution from Europe to Asia. The analysis of the transport
707 pathways and variations in PM mass and composition observed at the two sites in CA
708 demonstrate that this region is strategically located to characterize regional and intercontinental
709 transport of pollutants. Aerosols at these sites were shown to reflect dust, biomass burning, and
710 anthropogenic sources from South, East, and CA, Europe, and Russia depending on the time of
711 year. For example, during the spring fine particles from Europe and Africa were transported to
712 CA, on to eastern Asia, and then across the Pacific to North America.

713 Observations of PM and its composition in this region are of growing importance as it is
714 estimated that $PM_{2.5}$ levels are likely to increase significantly in Central and South Asia and
715 western China over the next few decades. Simulations for a reference 2030 emission scenario

716 showed that BC concentrations had a larger relative increase than PM_{2.5} concentrations. This
717 suggests that health impacts and climate warming associated with these pollutants may increase
718 over the next decades unless additional control measures are implemented. Continued pollutant
719 observations in CA will help to characterize the changes that are rapidly taking place in the
720 region.

721 **5. Acknowledgements**

722
723 The US Environmental Protection Agency through its Office of Research and Development
724 funded this study and collaborated in the research described here as a component of the
725 International Science & Technology Center (ISTC) project # 3715 (Transcontinental Transport
726 of Air Pollution from Central Asia to the US). The University of Iowa activities were also
727 supported in part by the following grants: EPA (RD-83503701-0), NASA (NNX08AH56G),
728 NSF (1049140), NCCR (UL1RR024979) and Fulbright-CONICYT (15093810). Its contents are
729 solely the responsibility of the authors and do not necessarily represent the official views of the
730 funding institutions. This manuscript has been subjected to U.S. EPA review and approved for
731 publication.

732
733 **6. References**

- 734 Adhikary, B., Carmichael, G. R., Tang, Y., Leung, L. R., Qian, Y., Schauer, J. J., Stone, E. a.,
735 Ramanathan, V. and Ramana, M. V.: Characterization of the seasonal cycle of south Asian
736 aerosols: A regional-scale modeling analysis, *J Geophys Res*, 112(D22), D22S22,
737 doi:10.1029/2006JD008143 , 2007.
- 738 Anenberg, S. C., Schwartz, J., Shindell, D., Amann, M., Faluvegi, G., Klimont, Z., Maenhout,
739 G., Pozzoli, L., van Dingenen, R., Vignati, E., Emberson, L., Muller, N. Z., West, J. J., Williams,
740 M., Demkine, V., Hicks, W. K., Kuylenstierna, J., Raes, F., and Ramanathan, V.: Global air
741 quality and health co-benefits of mitigating near-term climate change through methane and black
742 carbon emission controls, *Environ. Health Perspect.*, 120, 831–839, 2012.
- 743 Bates, T. S., Anderson, T. L., Baynard, T., Bond, T., Boucher, O., Carmichael, G., Clarke, A.,
744 Erlick, C., Guo, H., Horowitz, L., Howell, S., Kulkarni, S., Maring, H., McComiskey, A.,
745 Middlebrook, A., Noone, K., O'Dowd, C. D., Ogren, J., Penner, J., Quinn, P. K.,
746 Ravishankara, A. R., Savoie, D. L., Schwartz, S. E., Shinozuka, Y., Tang, Y., Weber, R. J., and
747 Wu, Y.: Aerosol direct radiative effects over the northwest Atlantic, northwest Pacific, and North
748 Indian Oceans: estimates based on in-situ chemical and optical measurements and chemical
749 transport modeling, *Atmos. Chem. Phys.*, 6, 1657-1732, doi:10.5194/acp-6-1657-2006, 2006.
- 750 Bauer, S., D. Koch, N. Unger, S. M. Metzger, D. T. Shindell, and D. G. Streets: Nitrate aerosols
751 today and in 2030: a global simulation including aerosols and tropospheric ozone, *Atmos. Chem.*
752 *Phys.*, 7, 5043–5059, 2007
- 753 Carmichael, G. R., Adhikary, B., Kulkarni, S., D’Allura, A., Tang, Y., Streets, D., Zhang, Q.,
754 Bond, T. C., Ramanathan, V., Jamroensan, A., and Marrapu, P.: Asian aerosols: current and year
755 2030 distributions and implications to human health and regional climate change, *Environ. Sci.*
756 *Technol.*, 43, 5811–5817, 2009.
- 757 Chen, B., Sverdlik, L. G., Imashev, S. A., Solomon, P. A., Lantz, J., Schauer, J. J., Shafer, M.
758 M., Artamonova, M. S., and Carmichael, G.: Empirical relationship between particulate matter

759 and aerosol optical depth over Northern Tien-Shan, Central Asia, *Air Quality, Atmosphere &*
760 *Health*, 6.2, 358-396, doi: 10.1007/s11869-012-0192-5, 2012.

761

762 Chen, B. B., Imashev, S. A., Sverdlik, L. G., Solomon, P. A., Lantz, J., Schauer, J. J., Shafer, M.
763 M., Artamonova, M. S. and Carmichael, G. R.: Ozone Variations over Central Tien-Shan in
764 Central Asia and Implications for Regional Emissions Reduction Strategies, *Aerosol Air Qual*
765 *Res*, 13, 555–562 Available from: 10.4209/aaqr.2012.06.156, 2013.

766 Chung, C. E., Ramanathan, V., Carmichael, G., Kulkarni, S., Tang, Y., Adhikary, B., Leung, L.
767 R. and Qian, Y.: Anthropogenic aerosol radiative forcing in Asia derived from regional models
768 with atmospheric and aerosol data assimilation, *Atmos Chem Phys*, 10(13), 6007–6024,
769 doi:10.5194/acp-10-6007-2010, 2010.

770 D’Allura, A., Kulkarni, S., Carmichael, G. R., Finardi, S., Adhikary, B., Wei, C., Streets, D.,
771 Zhang, Q., Pierce, R. B., Al-Saadi, J. A., Diskin, G., Wennberg, P.: Meteorological and air
772 quality forecasting using the WRF–STEM model during the 2008 ARCTAS field campaign,
773 *Atmos. Environ.*, 45, 6901–6910, doi:10.1016/j.atmosenv.2011.02.073, 2011.

774 Denier van der Gon, H., Visschedijk, A., Droge, R., Mulder, M., Johansson, C., and Klimont, Z.:
775 A high resolution emission inventory of particulate elemental carbon and organic carbon for
776 Europe in 2005, 7th International Conference on Air Quality – Science and Application (Air
777 Quality 2009), Istanbul, 2009.

778 Emerson, J. W., Hsu, A., Levy, M. A., de Sherbinin, A., Mara, V., Esty, D. C., and Jaiteh, M.:
779 Environmental Performance Index and Pilot Trend Environmental Performance Index, Yale
780 Center for Environmental Law and Policy, New Haven, 2012

781 Freitas, S. R., Longo, K. M., Chatfield, R., Latham, D., Silva Dias, M. A. F., Andreae, M. O.,
782 Prins, E., Santos, J. C., Gielow, R. and Carvalho Jr., J. A.: Including the sub-grid scale plume
783 rise of vegetation fires in low resolution atmospheric transport models, *Atmos Chem Phys* ,
784 7(13), 3385–3398, doi:10.5194/acp-7-3385-2007 , 2007.

785 Freitas, S. R., Longo, K. M., Trentmann, J. and Latham, D.: Technical Note: Sensitivity of 1-D
786 smoke plume rise models to the inclusion of environmental wind drag, *Atmos Chem Phys*, 10(2),
787 585–594, doi:10.5194/acp-10-585-2010, 2010.

788 Ginoux, P., Chin, M., Tegen, I., Prospero, J. M., Holben, B., Dubovik, O. and Lin, S.-J.: Sources
789 and distributions of dust aerosols simulated with the GOCART model, *J Geophys Res-Atmos*,
790 106(D17), 20255–20273, doi:10.1029/2000JD000053, 2001.

791 Gong, S. L.: A parameterization of sea-salt aerosol source function for sub- and super-micron
792 particles, *Global Biogeochem. Cy.* , 17(4), 1097, doi:10.1029/2003GB002079 , 2003.

793 Grell, G. A., Peckham, S. E., Schmitz, R., McKeen, S. A., Frost, G., Skamarock, W. C., and
794 Eder, B.: Fully coupled “online” chemistry within the WRF model, *Atmos. Environ.* 39, 6957–
795 6975, 2005.

796 Grell, G., Freitas, S. R., Stuefer, M., and Fast, J.: Inclusion of biomass burning in WRF-Chem:
797 impact of wildfires on weather forecasts, *Atmos. Chem. Phys.*, 11, 5289–5303, doi:10.5194/acp-
798 11-5289-2011, 2011.

799 Guttikunda, S., Tang, Y., Carmichael, G., Kurata, G., Pan, L., Streets, D., Woo, J.-H.,
800 Thongboonchoo, N., and Fried, A.: Impacts of Asian megacity emissions on regional air quality
801 during spring 2001, *J. Geophys. Res.*, 110, D20301, doi:10.1029/2004JD004921, 2005.

802 Hsu, N. C., Tsay, S.-C., King, M. D. and Herman, J. R.: Aerosol properties over bright-reflecting
803 source regions, *IEEE T Geosci Remote* , 42(3), 557–569, doi:10.1109/TGRS.2004.824067,
804 2004.

805 Hsu, N. C., Tsay, S.-C., King, M. D. and Herman, J. R.: Deep Blue Retrievals of Asian Aerosol
806 Properties During ACE-Asia, *IEEE T Geosci Remote* , 44(11), 3180–3195,
807 doi:10.1109/TGRS.2006.879540, 2006.

808 Huang, M., G. Carmichael, S. Kulkarni, D. Streets, Z. Lu, Q. Zhang, B. Pierce, Y. Kondo, J.
809 Jimenez-Palacios, M. J. Cubison, B. E. Anderson, and A. Wisthaler: Sectoral and geographical
810 contributions to summertime continental United States (CONUS) black carbon spatial
811 distributions, *Atmos. Environ.*, 51, 165-174, doi:10.1016/j.atmosenv.2012.01.021,2012

812 HTAP: Hemispheric Transport of Air Pollution 2010 (Executive Summary). Available online
813 from: http://www.htap.org/publications/2010_report/2010_Final_Report/EBMeeting2010.pdf
814 (Accessed 26 February 2013), 2010.

815 Hubanks, P. A., King, M. A., Platnick, S., and Pincus, R.: MODIS atmosphere L3 gridded
816 product algorithm theoretical basis document, MODIS Algorithm Teoretical Basis Document
817 No. ATBD-MOD-30 ,available at: [http://modis-
818 atmos.gsfc.nasa.gov/_docs/L3_ATBD_2008_12_04.pdf](http://modis-atmos.gsfc.nasa.gov/_docs/L3_ATBD_2008_12_04.pdf),2008.

819 Koch, D., Schulz, M., Kinne, S., McNaughton, C., Spackman, J. R., Balkanski, Y., Bauer, S.,
820 Berntsen, T., Bond, T. C., Boucher, O., Chin, M., Clarke, A., De Luca, N., Dentener, F.,
821 Diehl, T., Dubovik, O., Easter, R., Fahey, D. W., Feichter, J., Fillmore, D., Freitag, S., Ghan, S.,
822 Ginoux, P., Gong, S., Horowitz, L., Iversen, T., Kirkevåg, A., Klimont, Z., Kondo, Y., Krol, M.,
823 Liu, X., Miller, R., Montanaro, V., Moteki, N., Myhre, G., Penner, J. E., Perlwitz, J., Pitari, G.,
824 Reddy, S., Sahu, L., Sakamoto, H., Schuster, G., Schwarz, J. P., Seland, Ø., Stier, P.,
825 Takegawa, N., Takemura, T., Textor, C., van Aardenne, J. A., and Zhao, Y.: Evaluation of black
826 carbon estimations in global aerosol models, *Atmos. Chem. Phys.*, 9, 9001-9026,
827 doi:10.5194/acp-9-9001-2009, 2009

828

829 Kurata, G., Carmichael, G. R., Streets, D. G., Kitada, T., Tang, Y., Woo, J. H., and
830 Thongboonchoo, N.: Relationships between emission sources and air mass characteristics in East
831 Asia during the TRACE-P period, *Atmos. Environ.*, 38(40), 6977–6987, 2004.

832 Levy, R. C., Remer, L. A., Mattoo, S., Vermote, E. F. and Kaufman, Y. J.: Second-generation
833 operational algorithm: Retrieval of aerosol properties over land from inversion of Moderate
834 Resolution Imaging Spectroradiometer spectral reflectance, *J Geophys Res-Atmos* , 112(D13),
835 D13211, doi:10.1029/2006JD007811, 2007.

836 Lu, Z., Zhang, Q. and Streets, D. G.: Sulfur dioxide and primary carbonaceous aerosol emissions
837 in China and India, 1996–2010, *Atmos Chem Phys*, 11(18), 9839–9864, doi:10.5194/acp-11-
838 9839-2011 Available online from: <http://www.atmos-chem-phys.net/11/9839/2011/>, 2011.

839 Miller-Schulze, J. P., Shafer, M. M., Schauer, J. J., Solomon, P. a., Lantz, J., Artamonova, M.,
840 Chen, B., Imashev, S., Sverdlik, L., Carmichael, G. R. and Deminter, J. T.: Characteristics of
841 fine particle carbonaceous aerosol at two remote sites in Central Asia, *Atmos Environ*, 45(38),
842 6955–6964, doi:10.1016/j.atmosenv.2011.09.026, 2011.

843
844 Park, S., Martin M. Shafer, James J. Schauer, Paul A. Solomon, Jeffrey Lantz, Maria
845 Artamonova, Boris Chen, Sanjar Imashev, Leonid Sverdlik, Greg R. Carmichael: Chemical
846 characteristics, dynamics and provenance of mineral dust observed at two sites in Central Asia,
847 *Atmos. Environ.*, in preparation, 2014.

848 Ramanathan, V. and Carmichael, G.: Global and regional climate changes due to black carbon,
849 *Nat Geosci*, 1(4), 221–227 Available online from:
850 <http://www.nature.com/ngeo/journal/vaop/ncurrent/full/ngeo156.html> (Accessed 18 February
851 2013), 2008.

852 Remer, L. A., Kaufman, Y. J., Tanré, D., Mattoo, S., Chu, D. A., Martins, J. V, Li, R.-R., Ichoku,
853 C., Levy, R. C., Kleidman, R. G., Eck, T. F., Vermote, E., and Holben, B.N.: The MODIS
854 aerosol algorithm products and validation, *J. Atmos. Sci.*, 62, 947–973, doi:10.1175/JAS3385.1,
855 2005.

856 Skamarock, W. C., Klemp, J. B., Dudhia, J., Gill, D. O., Barker, D. M., Duda, M. G., Huang,
857 X.- Y., Wang, W., and Powers, J. G.: A Description of the Advanced Research WRF, Version 3.
858 Technical Report NCAR/TN475+ST R. National Center for Atmospheric Research Technical
859 Note, Boulder, Colorado, 2008.

860 Shindell, D., Kuylenstierna, J. C. I., Vignati, E., van Dingenen, R., Amann, M., Klimont, Z.,
861 Anenberg, S. C., Muller, N., Janssens-Maenhout, G., Raes, F., Schwartz, J., Faluvegi, G., Pozzoli,
862 L, Kupiainen, K., Hoglund-Isaksson, L., Emberson, L., Streets, D., Ramanathan, V., Hicks, K.,
863 Kim Oanh, N. T., Milly, G., Williams, M., Demkine, V., and Fowler, D: Simultaneously
864 mitigating near-term climate change and improving human health and food security, *Science*,
865 335, 183–189, doi:10.1126/science.1210026 , 2012.

866 UNEP: Framework Convention on Environmental Protection for Sustainable Development in
867 Central Asia, Regional Resource Centre for Asia and the Pacific (PRC.AP), available at:
868 <http://www.rrcap.ait.asia/library/ca-report/Brief-Convention.doc>, (last access: 25 April 2014),
869 2006.

870 UNEP and WMO: Integrated Assessment of Black Carbon and Tropospheric Ozone: Summary
871 for Decision Makers. available at:
872 http://www.unep.org/dewa/Portals/67/pdf/BlackCarbon_SDM.pdf (last access: 26 February
873 2013), 2011.

874 Uno, I., Satake, S., Carmichael, G. R., Tang, Y., Wang, Z., Takemura, T., Sugimoto, N.,
875 Shimizu, A., Murayama, T., Cahill, T.A., Cliff, S., Uematsu, M., Ohta, S., Quinn, P. K., and
876 Bates, T.S.: Numerical study of Asian dust transport during the springtime of 2001 simulated
877 with the Chemical Weather Forecasting System (CFORS) model, *J. Geophys. Res.*,
878 109(D19S24), doi:10.1029/2003JD004222, 2004.

879 V Visschedijk, A., Denier van der Gon, H., Droge, R., van der Brugh, H.: A European high
880 resolution and size-differentiated emission inventory for elemental and organic carbon for the
881 year 2005, TNO-034-UT-2009-00688_RPT-ML, TNO, Utrecht, 2009

882 Wang, W., Bruyere, C., Duda, M., Dudhia, J., Gill, D., Lin, H.-C., Michalakes, J., Rizvi, S. and
883 Zhang, X.: Version 3 Modeling System User ' s Guide January 2011, National Center for
884 Atmospheric Research (NCAR), available at:
885 http://www.mmm.ucar.edu/wrf/users/docs/user_guide_V3.2/ARWUsersGuideV3.pdf (last
886 access: 25 April 2014), 2011.

887 Wesely, M. L. and Hicks, B. B.: A review of the current status of knowledge on dry deposition,
888 *Atmos Environ*, 34(12–14), 2261–2282, doi:[http://dx.doi.org/10.1016/S1352-2310\(99\)00467-7](http://dx.doi.org/10.1016/S1352-2310(99)00467-7),
889 2000.

890 Whish-Wilson, P.: The Aral Sea environmental health crisis the desiccation of the Aral Sea
891 health in the Aral Sea region, *Journal of Rural and Remote Environmental Health*, 1(2), 29–34,
892 available at: <http://www.jcu.edu.au/jrtrph/vol/v01whish.pdf> (last access: 25 April 2014), 2002.

893 Wiedinmyer, C., Akagi, S. K., Yokelson, R. J., Emmons, L. K., Al-Saadi, J. a., Orlando, J. J.
894 and Soja, a. J.: The Fire INventory from NCAR (FINN): a high resolution global model to
895 estimate the emissions from open burning, *Geoscientific Model Development*, 4(3), 625–641,
896 doi:10.5194/gmd-4-625-2011, 2011.

897 Zhang, Q., Streets, D. G., Carmichael, G. R., He, K. B., Huo, H., Kannari, A., Klimont, Z., Park,
898 I. S., Reddy, S., Fu, J. S., Chen, D., et al.: Asian emissions in 2006 for the NASA INTEX-B
899 mission., *Atmos Chem Phys*, 9(14/2), 5131–5153, doi:10.5194/acp-9-5131-2009, 2009.

900

901 **7. Table Captions**

902 Table:1 Summary of changes in Central Asia (CA) region (See figure 1 for CA region definition)
903 emissions and concentration under the future emission scenarios (See Sect. 3.9 for more details)

904

905 **8. Figure Captions**

906 Fig. 1. WRF-STEM modeling domain set up and source region definition used in the
907 simulations. Modeling analysis was done on the hemispheric scale. The black dotted rectangular
908 box denotes the subset of the modeling domain used in this analysis. The triangle and circle
909 markers denote locations of the LST and Bishkek observation sites. The anthropogenic source
910 regions are denoted by colored regions with the A notation: A1 (N. America), A2 (Europe), A3
911 (Russia), A4 (Middle East), A5 (Central Asia), A6 (China) and A7 (South + Southeast Asia).
912 The dust source regions are indicated by the magenta rectangles with the D notations: D1
913 (Africa), D2 (Middle East), D3 (Central Asia) and D4 (Western China). The biomass burning
914 sources regional boundaries are indicated by the long dashed black lines with B notations: B1 (N.
915 America i.e. region west of 25 W), B2 (Europe i.e. region west of 45E and 40 N and above), B3
916 (Siberia : i.e east of 45 E and 40 N and above) and B4 (South Asia i.e. below 40 N). The insert
917 shows the topography around the observation sites.

918 Fig. 2. Spatial distribution of a) BC b) SO₂ c) Natural dust d) Biomass burning PM_{2.5} emissions
919 averaged over the simulation period in Gg/yr/grid.

920 Fig. 3. Spatial distribution of MODIS AOD averaged over the simulation period. The triangle
921 and circle markers denote the location of LST and Bishkek sites. The numbers on the map denote
922 contour values at sharp gradients.

923 Fig. 4. Spatial distribution of simulated a) BC ($\mu\text{g}/\text{m}^3$), b) Dust ($\mu\text{g}/\text{m}^3$), c) PM_{2.5} ($\mu\text{g}/\text{m}^3$), and d)
924 AOD averaged over the simulation period. The values on the map denote contour values at sharp
925 gradients.

926 Fig. 5. Comparison of predicted meteorological variables from WRF model with observations
927 shown as box and whisker plots over the simulation period (a) Temperature (K), (b) Relative
928 Humidity RH (%), (c) Wind Speed (m/s), (d) Wind Direction ($^\circ$), and (e) PBL height (m). Lidar
929 denotes the LST (Lidar Station Teplokluchenka) site. In each box whisker panel, the middle line
930 denotes the median value, while the edges of the box represent 25th and 75th percentile values
931 respectively. The whiskers denote the maximum and minimum values.

932 Fig. 6. Comparison of predicted aerosols with observations shown as box and whisker plots over
933 the simulation period at a) LST and b) Bishkek sites. SP and LE denote the AOD from the sun-
934 photometer (SP) and integrated from the vertical extinction profiles (LE). OBS and TEOM
935 denote filter and TEOM measurements while the MDL denotes the modeled values respectively.
936 Lidar denotes the LST (Lidar Station Teplokluchenka) site. In each box whisker panel, the
937 middle line denotes the median value, while the edges of the box represent 25th and 75th

938 percentile values respectively. The whiskers denote the maximum and minimum values. The
939 triangle marker denotes the mean value.

940 Fig. 7. Summary of period mean contributions by source regions and sectors for AOD, PM_{2.5},
941 dust, non-dust PM_{2.5}, sulfate and BC in % for the grid cells containing the Bishkek and LST
942 observation sites, and spatially averaged over the Central Asia region. See Fig. 1 for
943 anthropogenic, dust and fire source regions. Lidar denotes the LST (Lidar Station
944 Teplokluchenka) site.

945 Fig. 8. Temporal variability in simulated AOD compared with observations at the LST site. The
946 box-plots of monthly values are shown. AOD from the sun-photometer (SP) and integrated from
947 the vertical extinction profiles (LE) are shown. MDL denotes modeled values. Lidar denotes the
948 LST (Lidar Station Teplokluchenka) site. In each box whisker panel, the middle line denotes the
949 median value, while the edges of the box represent 25th and 75th percentile values respectively.
950 The whiskers denote the maximum and minimum values.

951 Fig. 9. Comparison of simulated PM mass with filter-based observations at Central Asia sites (a)
952 PM_{2.5} (LST) along with TEOM non-volatile measurements, (b) PM_{2.5} (Bishkek), (c) PM₁₀ (LST),
953 and (d) PM₁₀ (Bishkek) in ($\mu\text{g}/\text{m}^3$). Lidar denotes the LST (Lidar Station Teplokluchenka) site.

954 Fig. 10. Temporal variability in simulated (a) Temperature (K) and (b) Relative Humidity RH
955 (%) from WRF model compared with observations at the LST and Bishkek sites. Lidar denotes
956 the LST (Lidar Station Teplokluchenka) site.

957 Fig. 11. Simulated composition of PM_{2.5} at the LST site by a) Species ($\mu\text{g}/\text{m}^3$), b) Fine dust
958 source regions($\mu\text{g}/\text{m}^3$) c) Anthropogenic PM_{2.5} source regions ($\mu\text{g}/\text{m}^3$) d) Anthropogenic PM_{2.5}
959 source ($\mu\text{g}/\text{m}^3$) e) Biomass PM_{2.5} source regions($\mu\text{g}/\text{m}^3$).The contributions from source region
960 and sectors denote the non – dust portion of PM_{2.5} mass.

961 Fig. 12. Simulated composition of BC at the LST site by a) Source regions ($\mu\text{g}/\text{m}^3$), b) Source
962 sector ($\mu\text{g}/\text{m}^3$), and c) Biomass burning source regions ($\mu\text{g}/\text{m}^3$).

963 Fig. 13. Time altitude cross sections of weekly averaged predicted BC, dust and PM_{2.5} for the
964 simulation period at the LST site. The numbers denote the specific episodes of aerosol
965 enhancements for back trajectory analysis in Fig. 14 and Fig. 15. Lidar denotes the LST (Lidar
966 Station Teplokluchenka) site.

967 Fig. 14. Ten day air mass back trajectories for August 2008 (events 1 and 2 as denoted in Fig.
968 13) color coded by source regions. The blue diamond and green square hatched areas denote the
969 natural dust and biomass burning emission sources while the number in black denote MODIS
970 AOD contours averaged over the event time period and ten day prior time window. The
971 trajectories are color coded by source regions including Africa (blue), Middle East (green),
972 Central Asia (yellow), North Asia biomass (> 50° N, black), Europe (brown), China (red) and
973 South Asia (orange). Lidar denotes the LST (Lidar Station Teplokluchenka) site.

974 Fig. 15. Same as Fig. 14 but for November 2008, January 2009 and April 2009 (events 3, 4, 5
975 denoted in Fig. 13).

976 Fig. 16 Ten day air mass forward trajectories illustrating the seasonality in transport pathways
977 out of CA for a) June 2008, b) December 2008, and c) April 2009. The blue diamond, green
978 square hatched areas denote the natural dust and biomass burning emission sources while the
979 number in black denote MODIS AOD contours, respectively, averaged over the event time
980 period and subsequent ten day time window. Lidar denotes the LST (Lidar Station
981 Teplokluchenka) site.

982 Fig. 17. Seasonally averaged surface total dust (PM_{10}) concentrations from Central Asia dust
983 emissions. DJF (top left panel) denotes the average for the months of December, January and
984 February. MAM (top right panel) denotes the average for months of March, April and May. JJA
985 (bottom left panel) denotes the average for months of June, July and August while SON (bottom
986 right panel) denotes average for months of September, October and November.

987 Fig. 18. Time series of predicted surface concentration at 6 h time step (top panel) and weekly
988 averaged time altitude cross sections (bottom panel) of total dust (PM_{10}) from Central Asia dust
989 emissions at Mt. Bachelor, Oregon.

990 Fig. 19. Percent change in simulated period mean surface BC and $PM_{2.5}$ concentrations for future
991 2030 emission scenarios relative to the base year (2005) a),d) reference 2030, a),e) BC measures
992 (low) and c),f) BC (lowest) and greenhouse gas measures aimed at keeping CO_2 levels below
993 450 ppm. Refer to Sec. 2.3 for more details on emission scenarios.

994

995 **9. Supplemental Materials Figure and Table Captions**

996 Table S1. Comparison of the observed and predicted surface meteorology at the observation
997 sites.

998 Table S2. Comparison of observations and model of AOD, $PM_{2.5}$, PM_{10} , BC and OC at the
999 Bishkek site.

1000 Table S3. Comparison of observations and model of AOD, $PM_{2.5}$, PM_{10} , BC and OC at the LST
1001 site.

1002

1003 Fig. S1. Seasonal variability in spatial distribution of biomass burning $PM_{2.5}$ emissions in
1004 Gg/month/grid (a) April 2008, (b) August 2008, (c) November 2008, and (d) May 2009.

1005 Fig. S2. Spatial distribution of a) base year 2005 BC emissions (Gg/yr/grid) along with percent
1006 change (w.r.t to base year 2005) in b) Reference 2030 BC emissions c) 2030 BC emissions with
1007 BC measures (low) and d) 2030 BC emissions with BC (lowest) and greenhouse gas measures
1008 aimed at keeping CO_2 levels below 450ppm. The triangle and circle markers denote locations of
1009 the LST and Bishkek sites. Refer to Sec. 2.3 for more details on emission scenarios.

1010 Fig. S3. Spatial distribution of a) base year 2005 $PM_{2.5}$ emissions (Gg/yr/grid) along with percent
1011 change (w.r.t to base year 2005) in b) Reference 2030 $PM_{2.5}$ emissions c) 2030 $PM_{2.5}$ emissions
1012 with BC measures and d) 2030 $PM_{2.5}$ emissions with BC and greenhouse gas measures aimed at

1013 keeping CO₂ levels below 450ppm. The triangle and circle markers denote locations of the LST
1014 and Bishkek sites. Refer to Sec. 2.3 for more details on emission scenarios.

1015 Fig. S4. Spatial distribution of a) base year 2005 SO₂ emissions (Gg/yr/grid) along with percent
1016 change (w.r.t to base year 2005) in (b) Reference 2030 SO₂emissions c) 2030 SO₂ emissions with
1017 BC measures and d) 2030 SO₂ emissions with BC and greenhouse gas measures aimed at
1018 keeping CO₂ levels below 450ppm. The triangle and circle markers denote locations of the LST
1019 and Bishkek sites. Refer to Sec. 2.3 for more details on emission scenarios.

1020 Fig. S5. Comparison of observed and predicted PBL heights (m) at the LST site. Observed PBL
1021 heights were determined from the Lidar profiles.

1022 Fig. S6. Spatial distribution of predicted species contributions (%) to AOD averaged over the
1023 simulation period a) Carbonaceous aerosols (BC+OC), b) SO₄, c) Other PM, and d) Dust.

1024 Fig. S7. Spatial distribution of predicted species contributions (%) to PM_{2.5} averaged over the
1025 simulation period a) Carbonaceous aerosols (BC+OC), b) SO₄, c) Other PM_{2.5}, and d) Dust.

1026 Fig. S8. Seasonal variability in spatial distribution of MODIS and simulated AOD averaged over
1027 the simulation period.

1028 Fig S9. Summary of period mean contributions by source regions and sectors for OC in % for the
1029 grid cells containing the Bishkek and LST observation sites, and spatially averaged over the
1030 Central Asia region. See Fig. 1 for anthropogenic and fire source regions.

1031 Table:1 Summary of changes in Central Asia (CA) region (See figure 1 for CA region definition)
 1032 emissions and concentration under the future emission scenarios (See Sect. 3.9 for more details)
 1033

| Emission Scenario | Emissions Gg yr ⁻¹ | | | Emissions change (%) w.r.t to base 2005 | | |
|-------------------------|-------------------------------|-----------------|------------------|---|-----------------|------------------|
| | BC | SO ₂ | PM ₂₅ | BC | SO ₂ | PM ₂₅ |
| Base 2005 | 39 | 1130 | 197 | | | |
| Reference 2030 | 47 | 1326 | 224 | 22.1 | 17.3 | 13.9 |
| Low GWP 2030 | 27 | 1325 | 177 | -31.1 | 17.3 | -10.1 |
| Lowest GWP + 450 | 21 | 1058 | 115 | -46.9 | -6.4 | -41.5 |

| Emission Scenario | Concentration (µg m ⁻³) | | | Concentration change (%) w.r.t to base 2005 | | |
|-------------------------|-------------------------------------|-----------------|------------------|---|-----------------|------------------|
| | BC | SO ₄ | PM ₂₅ | BC | SO ₄ | PM ₂₅ |
| Base 2005 | 0.17 | 3.04 | 4.26 | | | |
| Reference 2030 | 0.16 | 2.65 | 4.03 | -4.2 | -12.6 | -5.3 |
| Low GWP 2030 | 0.11 | 2.64 | 3.85 | -36.6 | -13 | -9.5 |
| Lowest GWP + 450 | 0.10 | 2.04 | 3.06 | -38.5 | -32.9 | -28 |

1034

1035

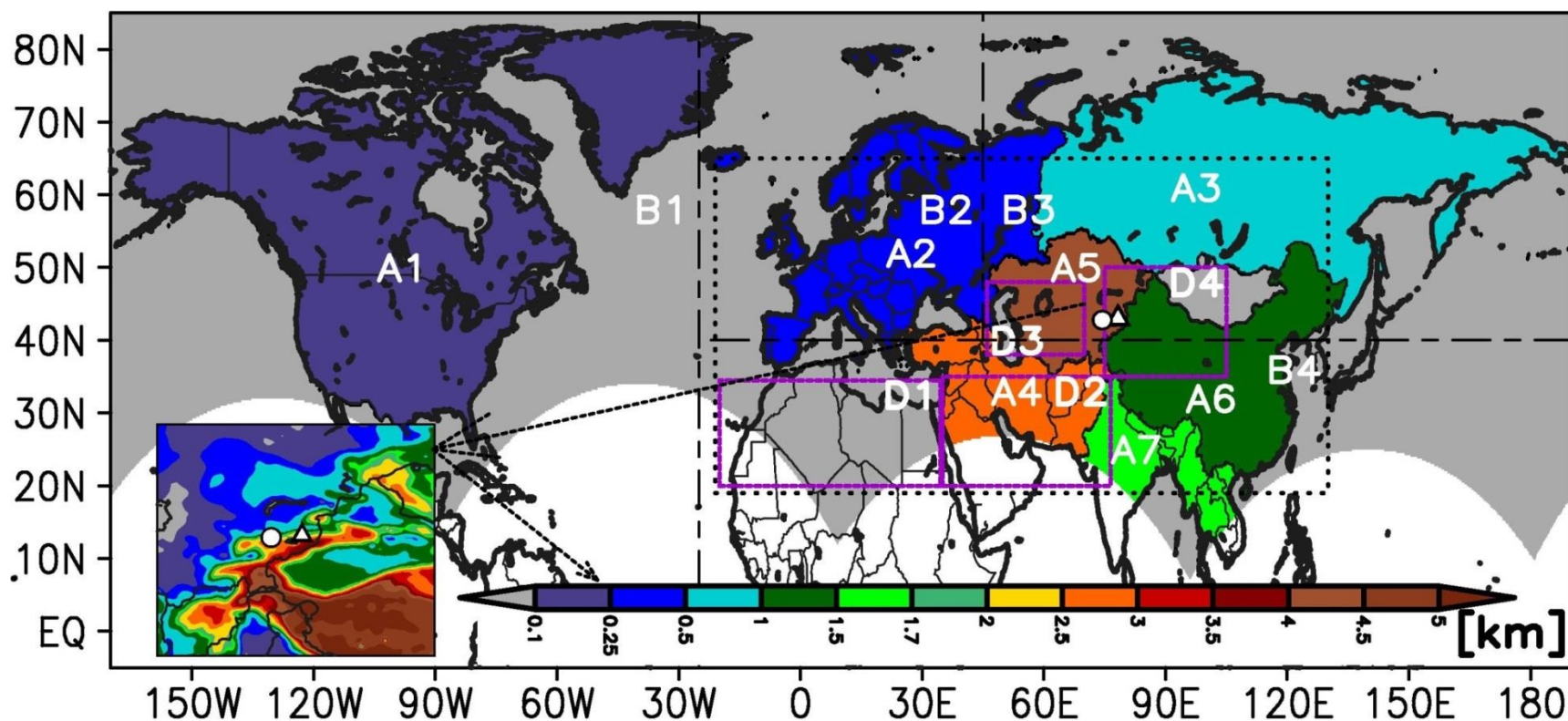


Fig. 1. WRF-STEM modeling domain set up and source region definition used in the simulations. Modeling analysis was done on the hemispheric scale. The black dotted rectangular box denotes the subset of the modeling domain used in this analysis. The triangle and circle markers denote locations of the LST and Bishkek observation sites. The anthropogenic source regions are denoted by colored regions with the A notation: A1 (N. America), A2 (Europe), A3 (Russia), A4 (Middle East), A5 (Central Asia), A6 (China) and A7 (South + Southeast Asia). The dust source regions are indicated by the magenta rectangles with the D notations: D1 (Africa), D2 (Middle East), D3 (Central Asia) and D4 (Western China). The biomass burning sources regional boundaries are indicated by the long dashed black lines with B notations: B1 (N. America i.e. region west of 25 W), B2 (Europe i.e. region west of 45E and 40 N and above), B3 (Siberia : i.e east of 45 E and 40 N and above) and B4 (South Asia i.e. below 40 N). The insert shows the topography around the observation sites.

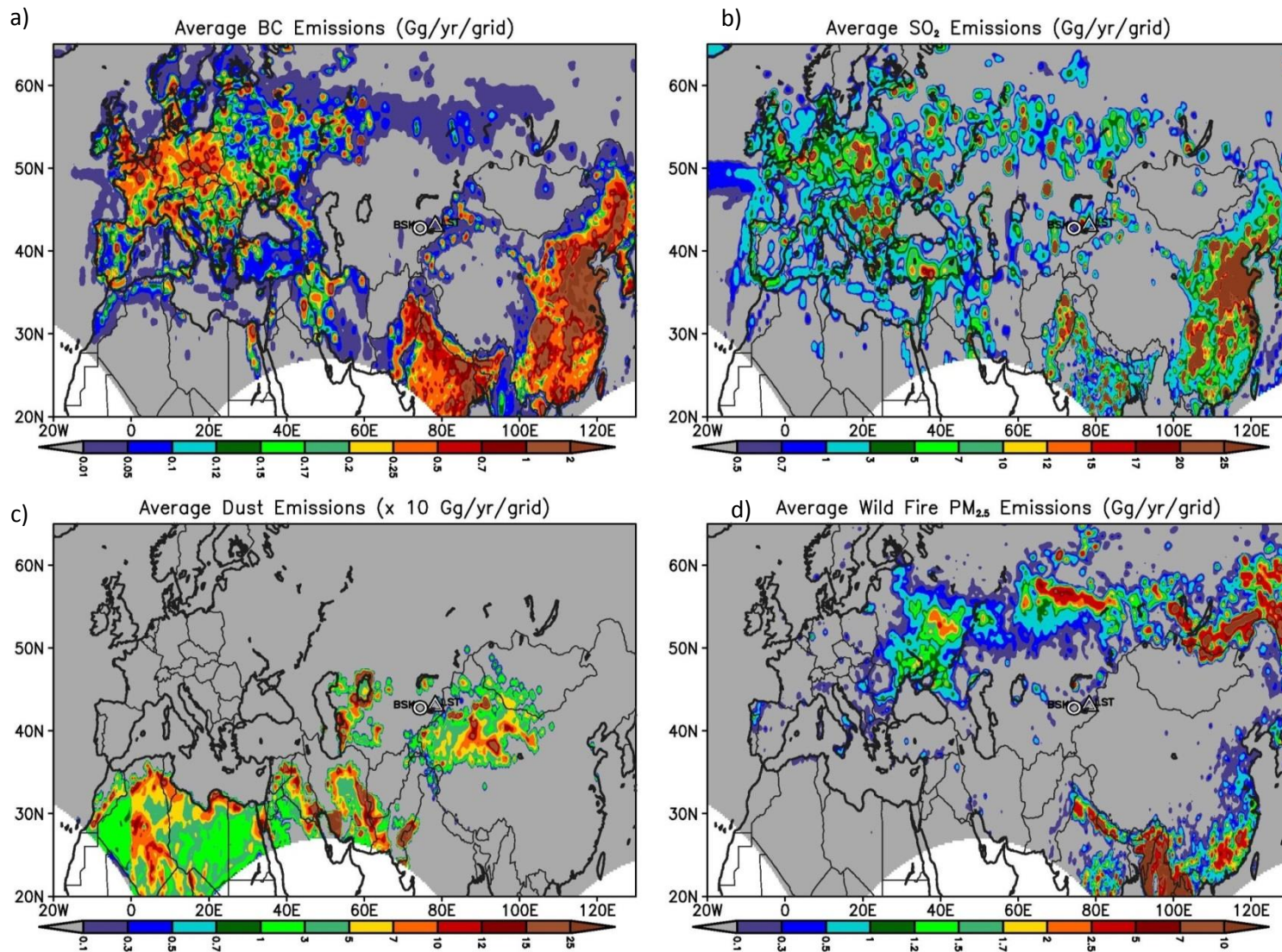


Fig. 2. Spatial distribution of a) BC b) SO₂ c) Natural dust d) Biomass burning PM_{2.5} emissions averaged over the simulation period in Gg/yr/grid.

Average MODIS AOD (April 2008 – July 2009)

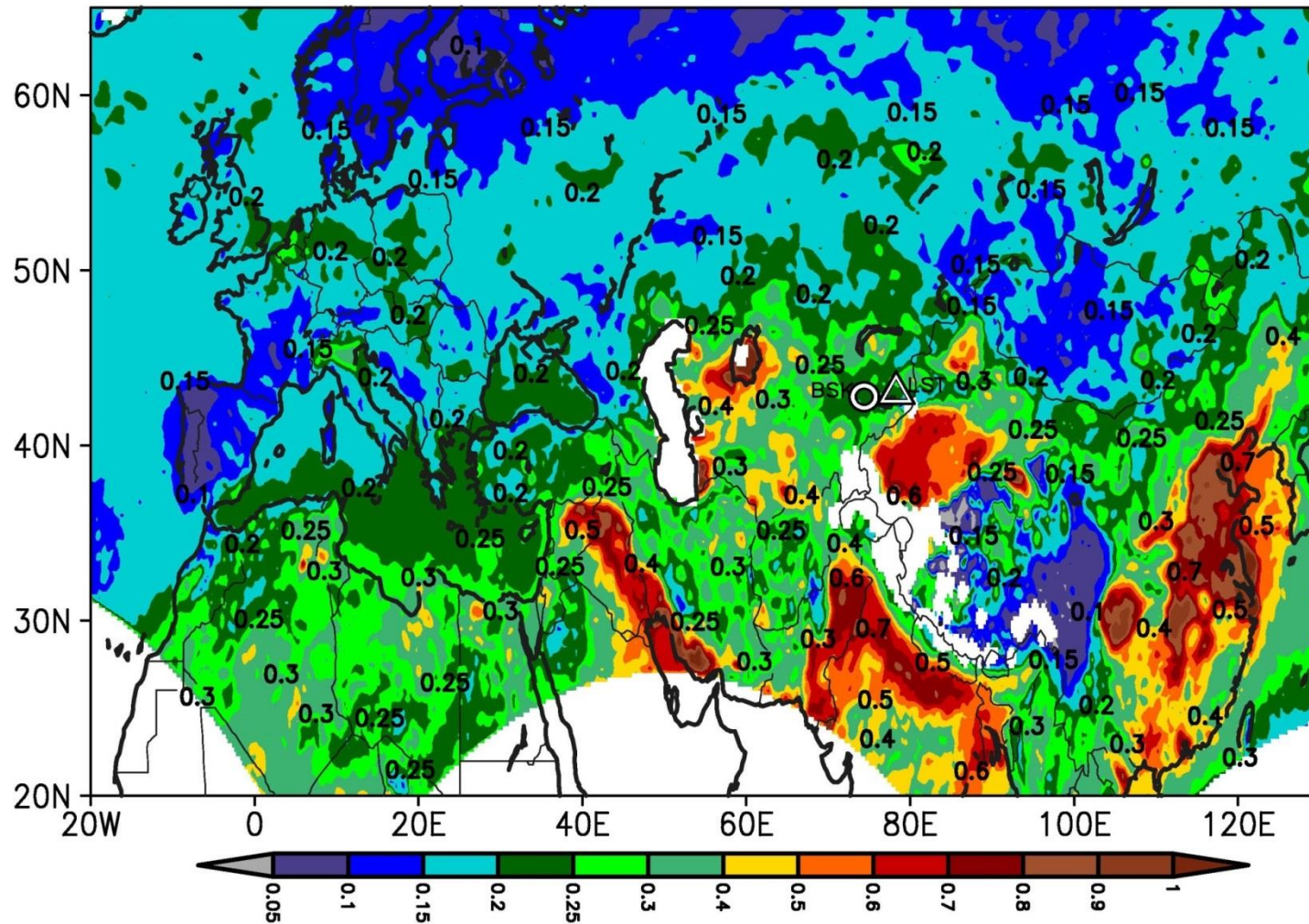


Fig. 3. Spatial distribution of MODIS AOD averaged over the simulation period. The triangle and circle markers denote the location of LST and Bishkek sites. The numbers on the map denote contour values at sharp gradients.

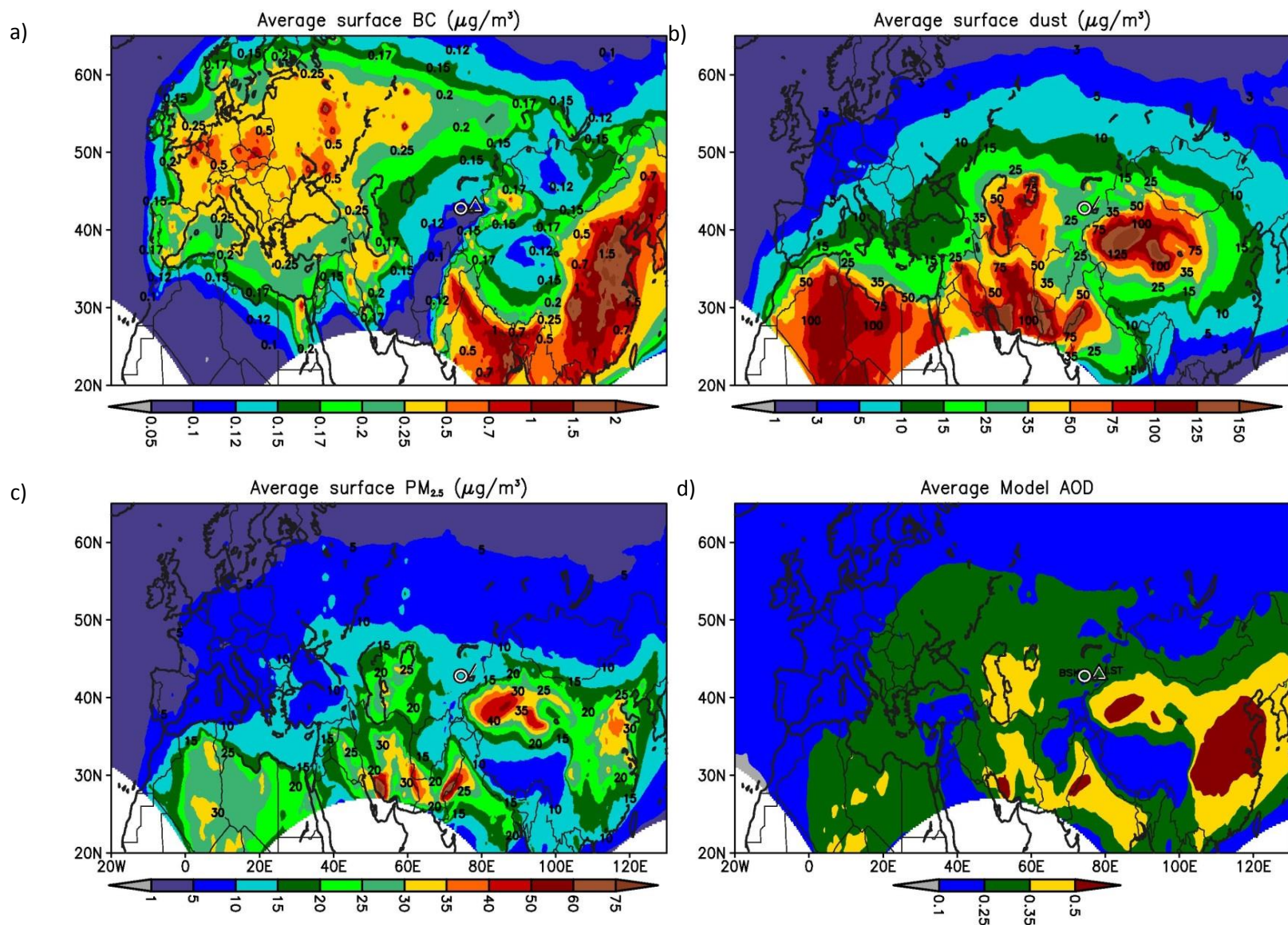


Fig. 4. Spatial distribution of simulated a) BC ($\mu\text{g}/\text{m}^3$), b) Dust ($\mu\text{g}/\text{m}^3$), c) PM_{2.5} ($\mu\text{g}/\text{m}^3$), and d) AOD averaged over the simulation period. The values on the map denote contour values at sharp gradients.

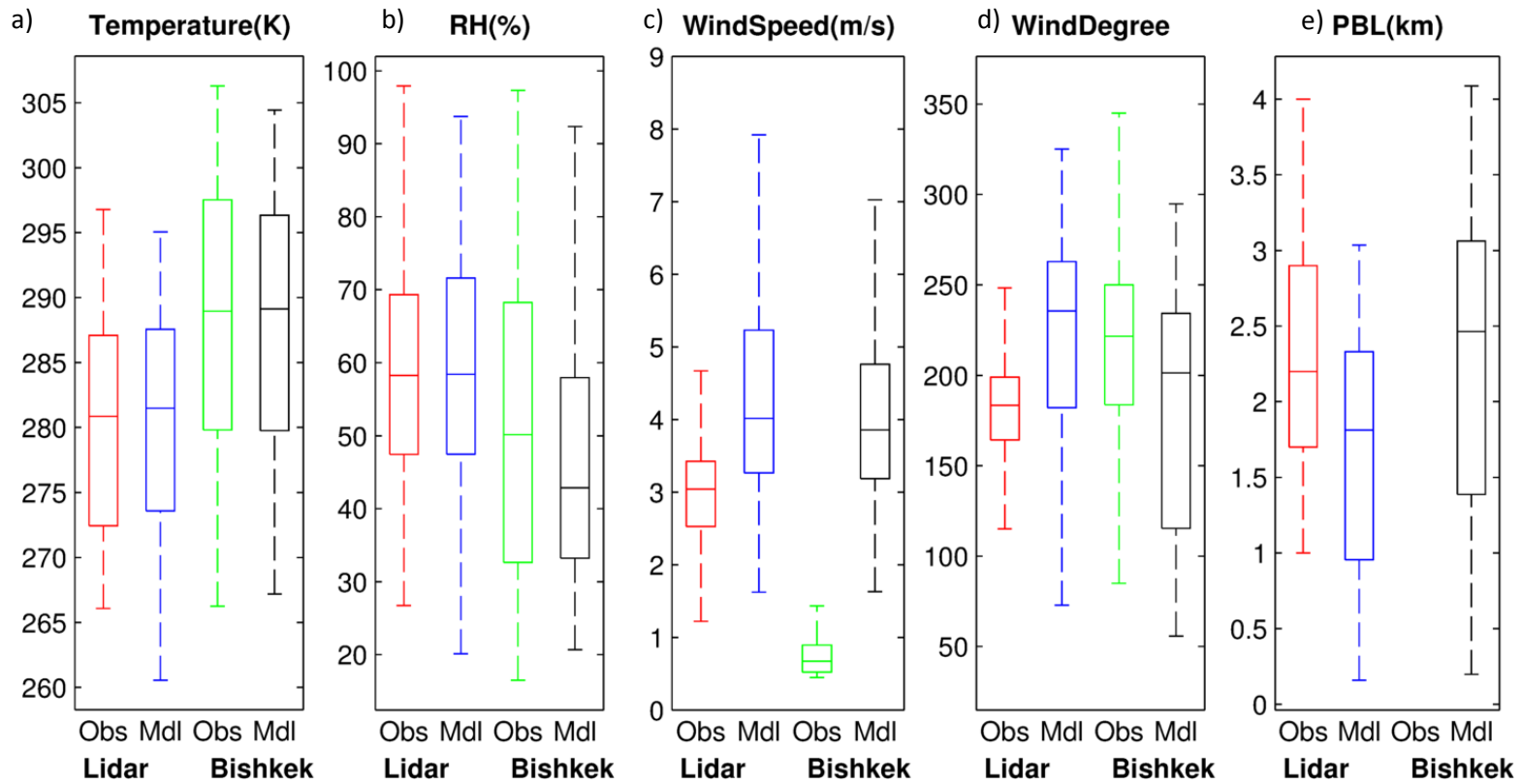


Fig. 5. Comparison of predicted meteorological variables from WRF model with observations shown as box and whisker plots over the simulation period (a) Temperature (K), (b) Relative Humidity RH (%), (c) Wind Speed (m/s), (d) Wind Direction ($^{\circ}$), and PBL height (m). Lidar denotes the LST (Lidar Station Teplokluchenska) site. In each box whisker panel, the middle line denotes the median value, while the edges of the box represent 25th and 75th percentile values respectively. The whiskers denote the maximum and minimum values.

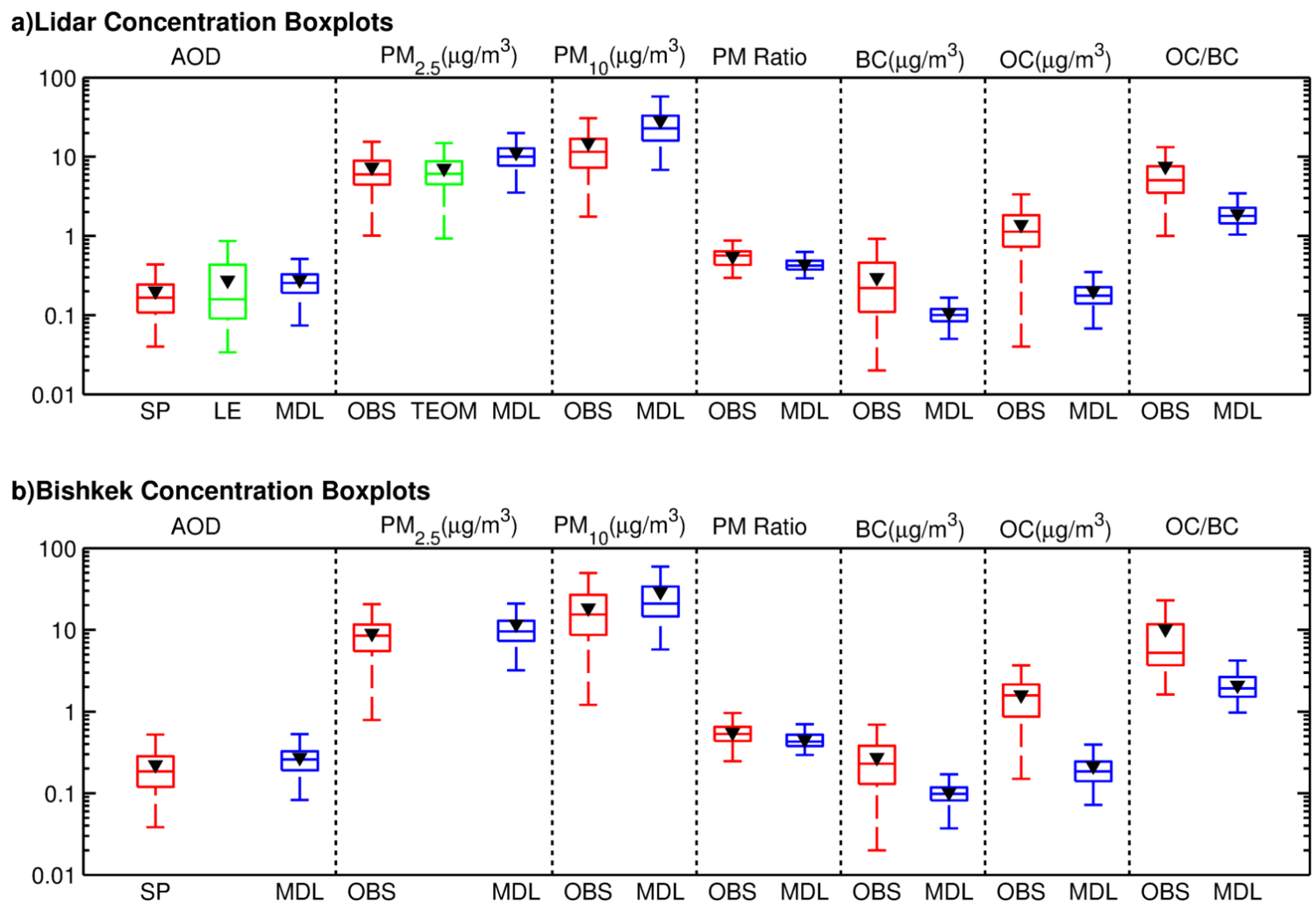


Fig. 6. Comparison of predicted aerosols with observations shown as box and whisker plots over the simulation period at a) LST and b) Bishkek sites. SP and LE denote the AOD from the sun-photometer (SP) and integrated from the vertical extinction profiles (LE). OBS and TEOM denote filter and TEOM measurements while the MDL denotes the modeled values respectively. Lidar denotes the LST (Lidar Station Teplokluchenska) site. In each box whisker panel, the middle line denotes the median value, while the edges of the

box represent 25th and 75th percentile values respectively. The whiskers denote the maximum and minimum values. The triangle marker denotes the mean value.

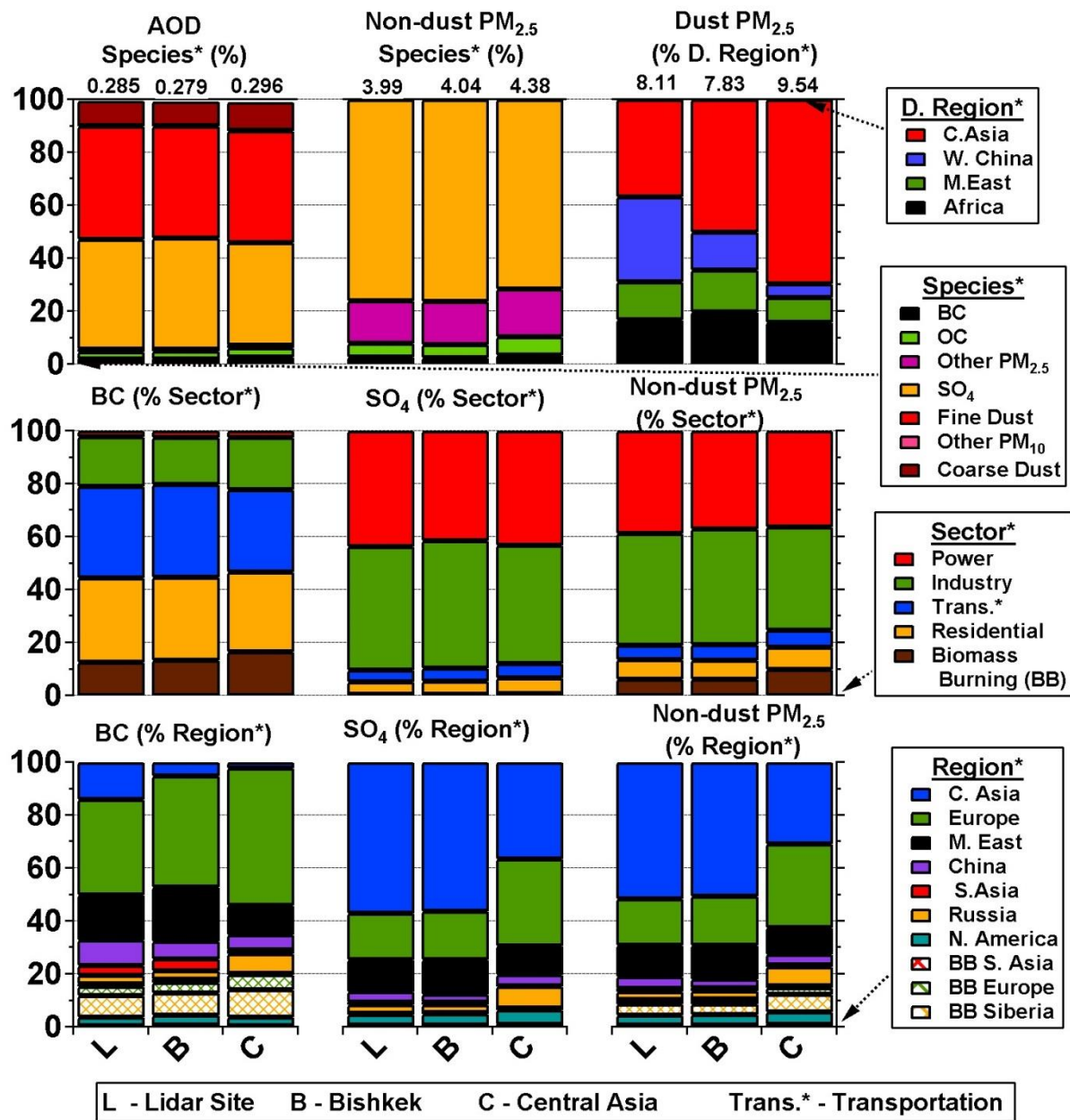


Fig. 7. Summary of period mean contributions by source regions and sectors for AOD, PM_{2.5}, dust, non-dust PM_{2.5}, sulfate and BC in % for the grid cells containing the Bishkek and LST observation sites, and spatially averaged over the Central Asia region. See Fig. 1 for anthropogenic, dust and fire source regions. Lidar denotes the LST (Lidar Station Teplokluhenka) site.

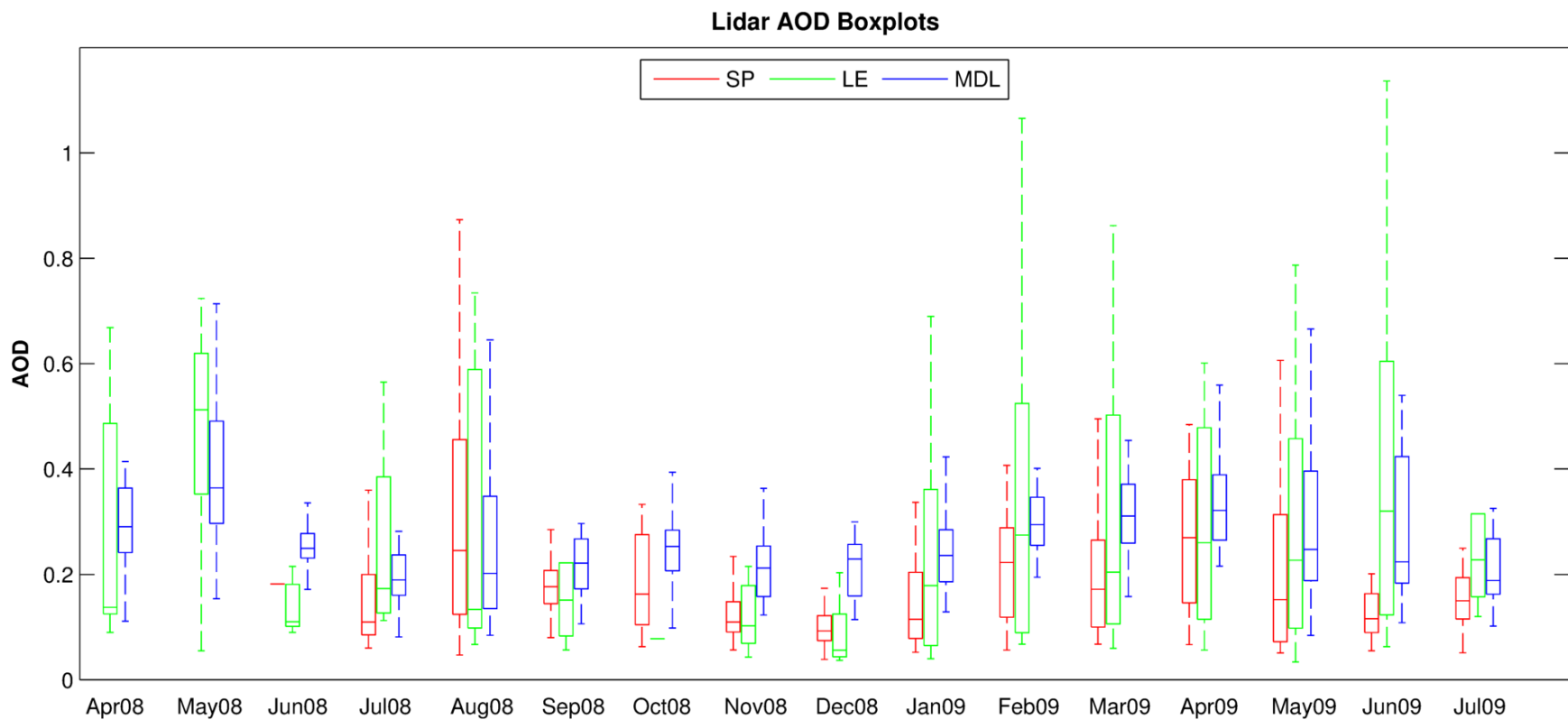


Fig. 8. Temporal variability in simulated AOD compared with observations at the LST site. The box-plots of monthly values are shown. AOD from the sun-photometer (SP) and integrated from the vertical extinction profiles (LE) are shown. MDL denotes modeled values. Lidar denotes the LST (Lidar Station Teplokluchenka) site. In each box whisker panel, the middle line denotes the median value, while the edges of the box represent 25th and 75th percentile values respectively. The whiskers denote the maximum and minimum values.

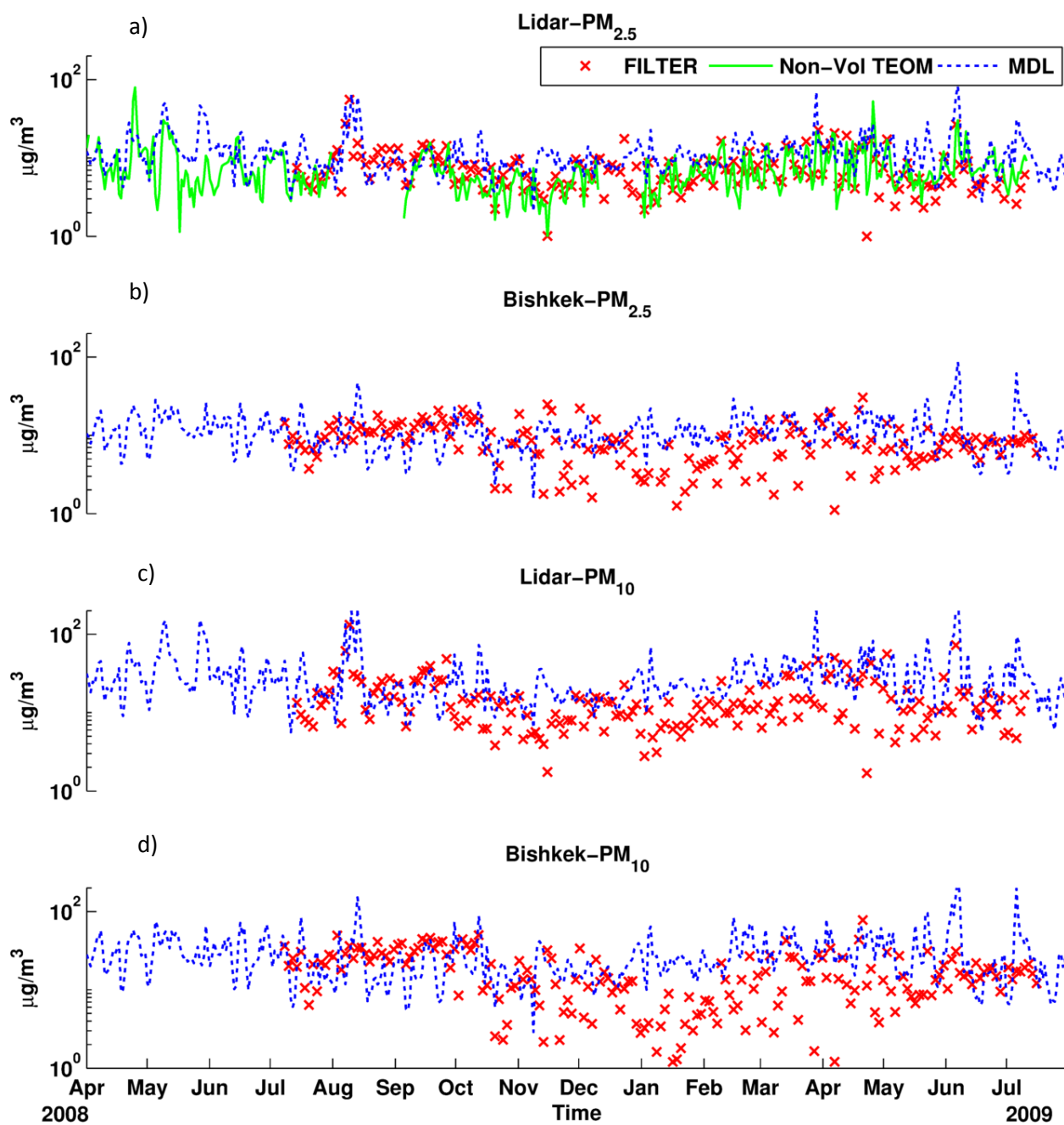


Fig. 9. Comparison of simulated PM mass with filter-based observations at Central Asia sites (a) PM_{2.5} (LST) along with TEOM non-volatile measurements, (b) PM_{2.5} (Bishkek), (c) PM₁₀ (LST), and (d) PM₁₀ (Bishkek) in ($\mu\text{g}/\text{m}^3$). Lidar denotes the LST (Lidar Station Teplokluchenka) site.

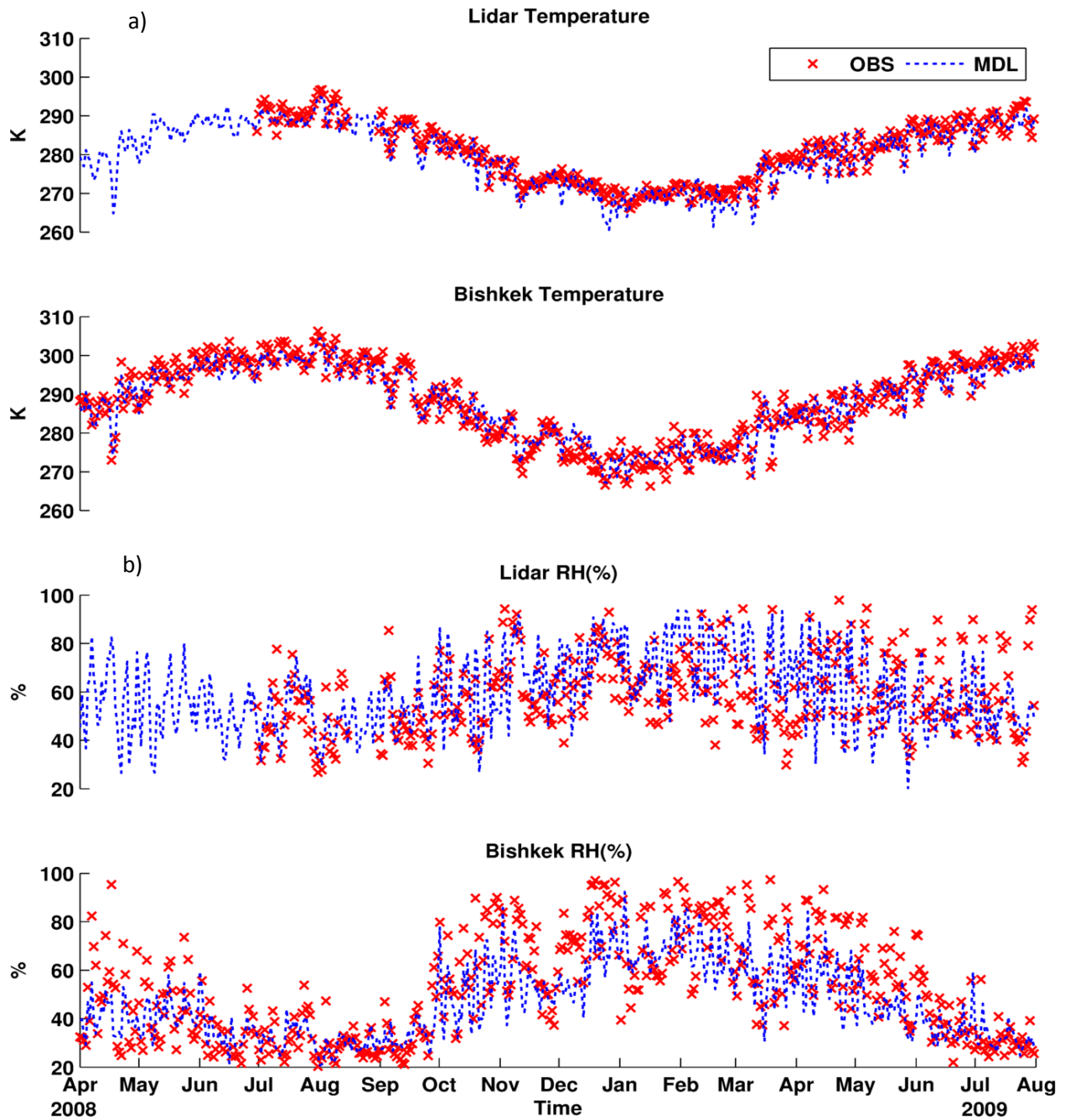


Fig. 10. Temporal variability in simulated Temperature (K) and (b) Relative Humidity RH (%) from WRF model compared with observations at the LST and Bishkek sites. Lidar denotes the LST (Lidar Station Teplokluchenka) site.

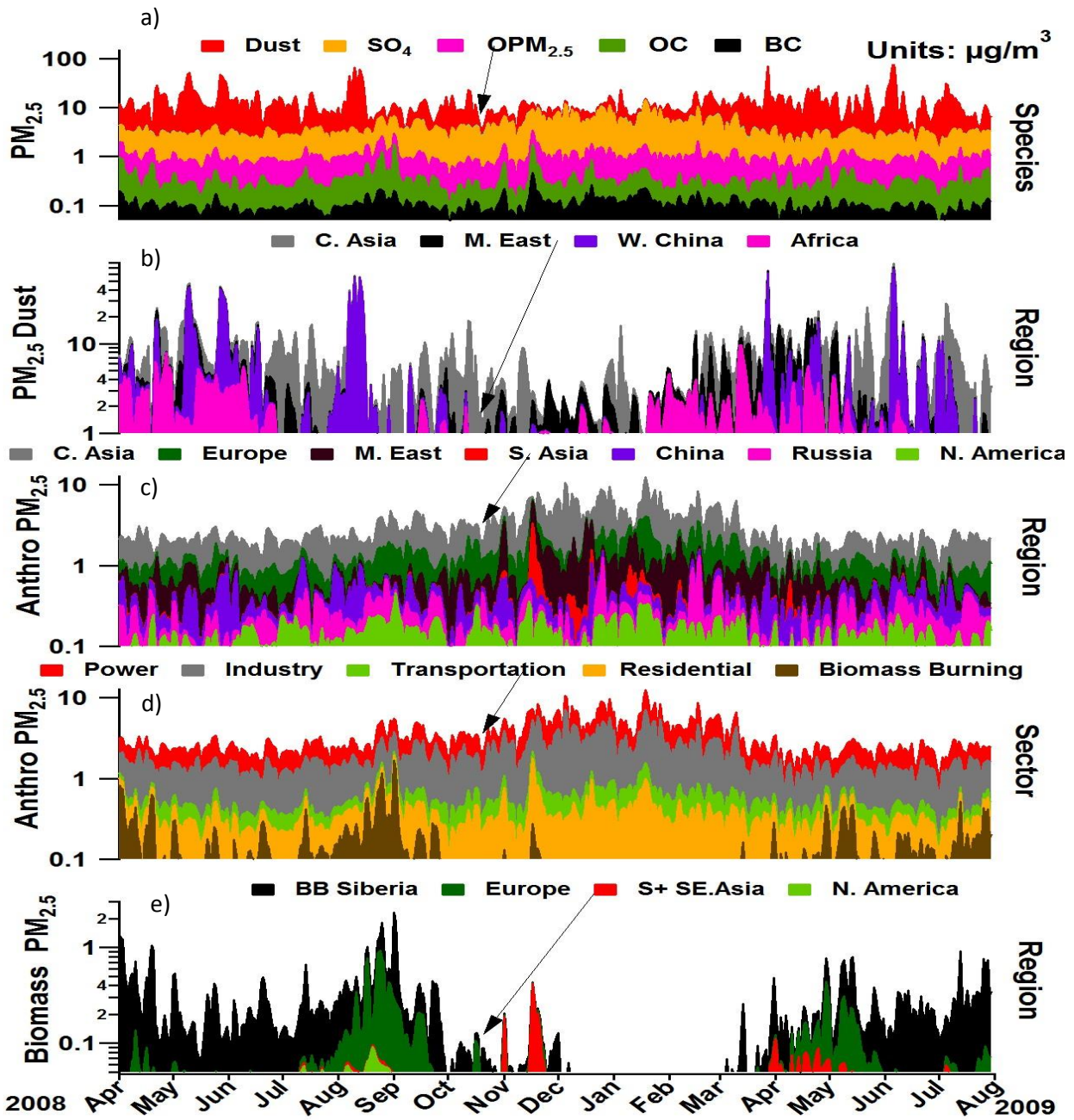


Fig. 11. Simulated composition of $PM_{2.5}$ at the LST site by a) Species ($\mu\text{g}/\text{m}^3$), b) Source sector ($\mu\text{g}/\text{m}^3$), and c) Source regions ($\mu\text{g}/\text{m}^3$). The contributions from source region and sectors denote the non – dust portion of $PM_{2.5}$ mass.

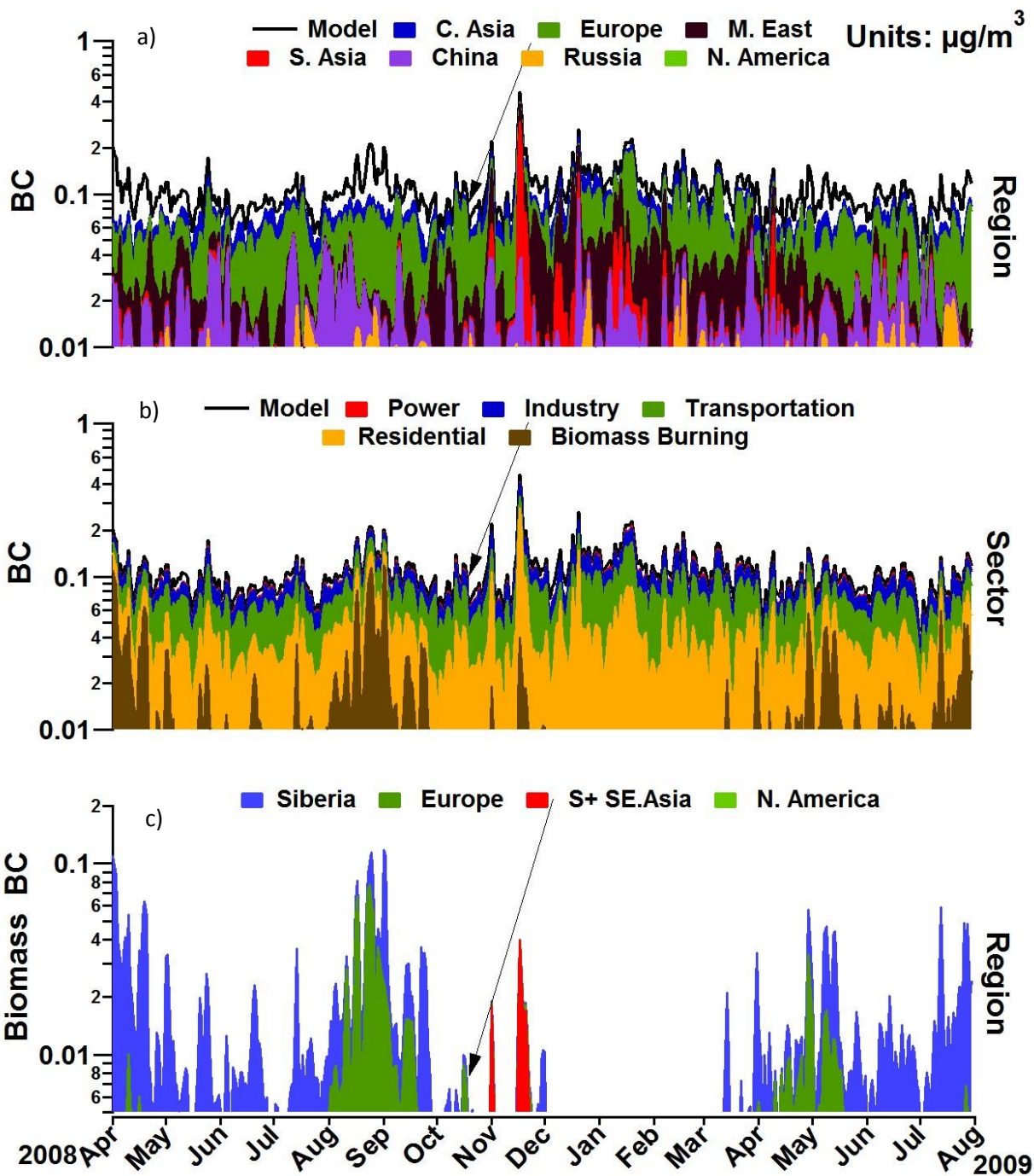


Fig. 12. Simulated composition of BC at the LST site by a) Source regions ($\mu\text{g}/\text{m}^3$), b) Source sector ($\mu\text{g}/\text{m}^3$), and c) Biomass burning source regions ($\mu\text{g}/\text{m}^3$).

Time Altitude Curtains at Lidar

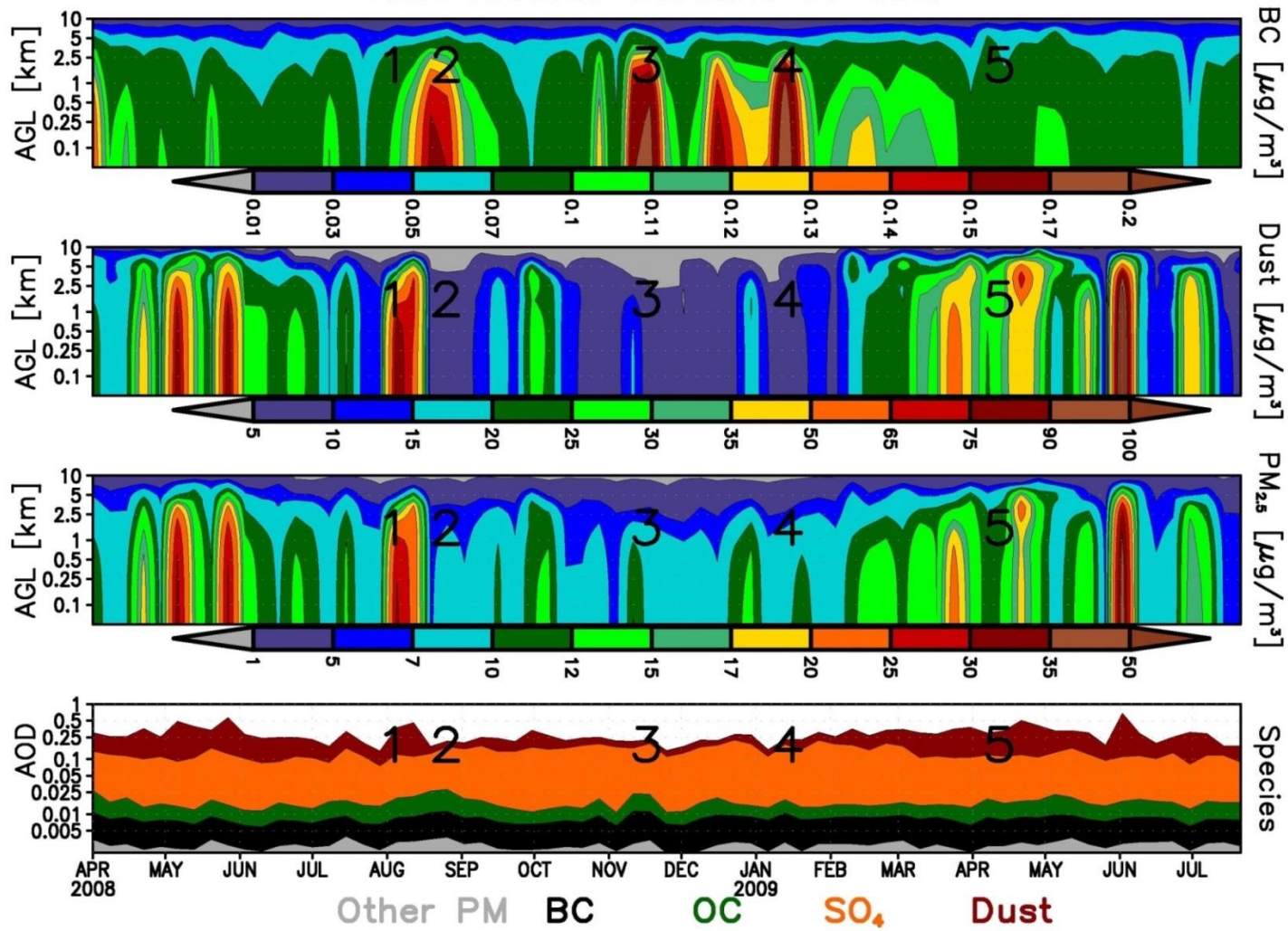


Fig. 13. Time altitude cross sections of weekly averaged predicted BC, dust and PM_{2.5} for the simulation period at the LST site. The numbers denote the specific episodes of aerosol enhancements for back trajectory analysis in Fig. 14 and Fig. 15. Lidar denotes the LST (Lidar Station Teplokluchenka) site.

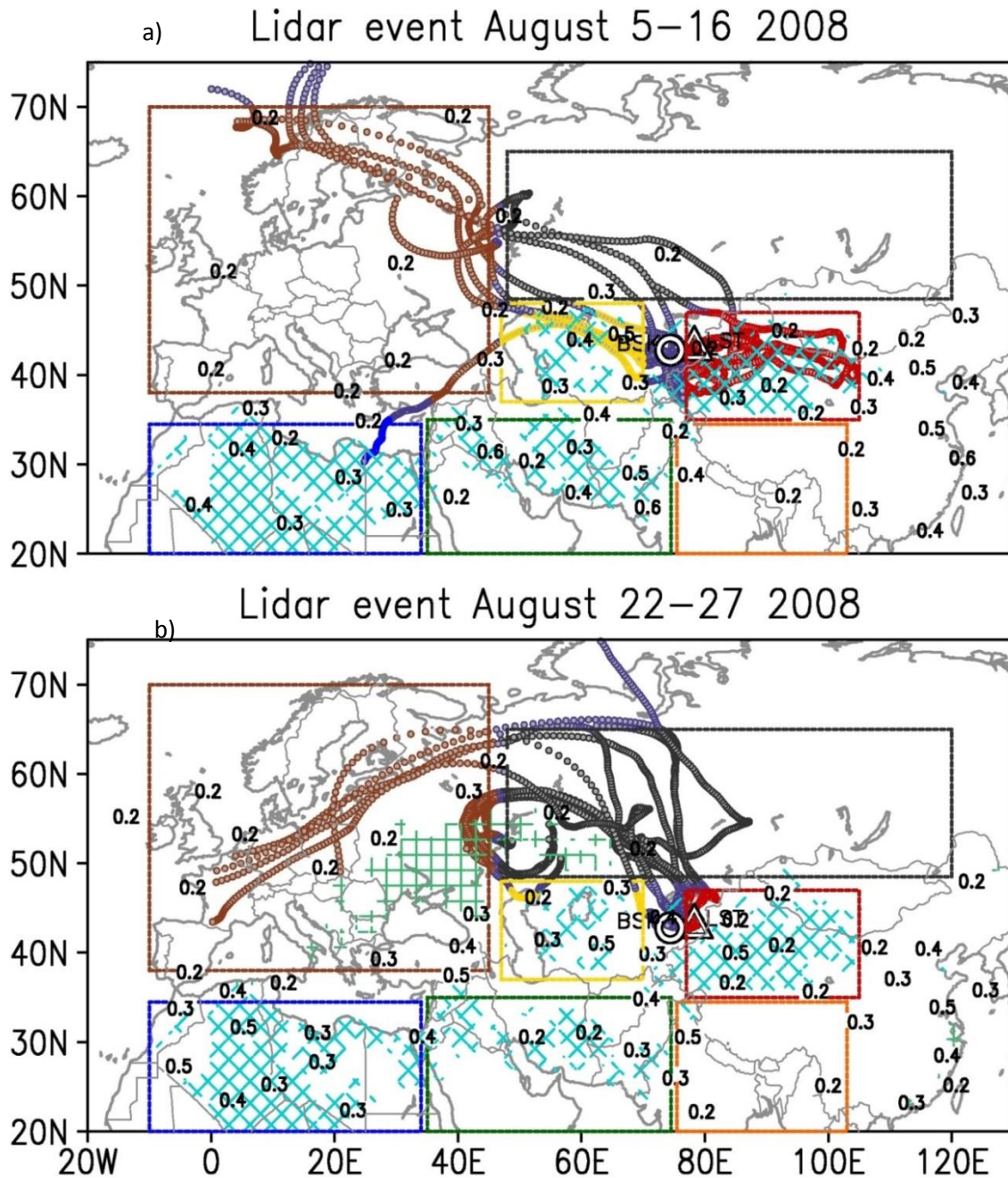


Fig. 14. Ten day air mass back trajectories for August 2008 (events 1 and 2 as denoted in Fig. 11) color coded by source regions. The blue diamond and green square hatched areas denote the natural dust and biomass burning emission sources while the number in black denote MODIS AOD contours averaged over the event time period and ten day prior time window. The trajectories are color coded by source regions including Africa (blue), Middle East (green), Central Asia (yellow), North Asia biomass ($> 50^\circ \text{N}$, black), Europe (brown), China (red) and South Asia (orange). (green), Central Asia (yellow), North Asia biomass ($> 50^\circ \text{N}$,

black), Europe (brown), China (red) and South Asia (orange). Lidar denotes the LST (Lidar Station Teplokluchenka) site.

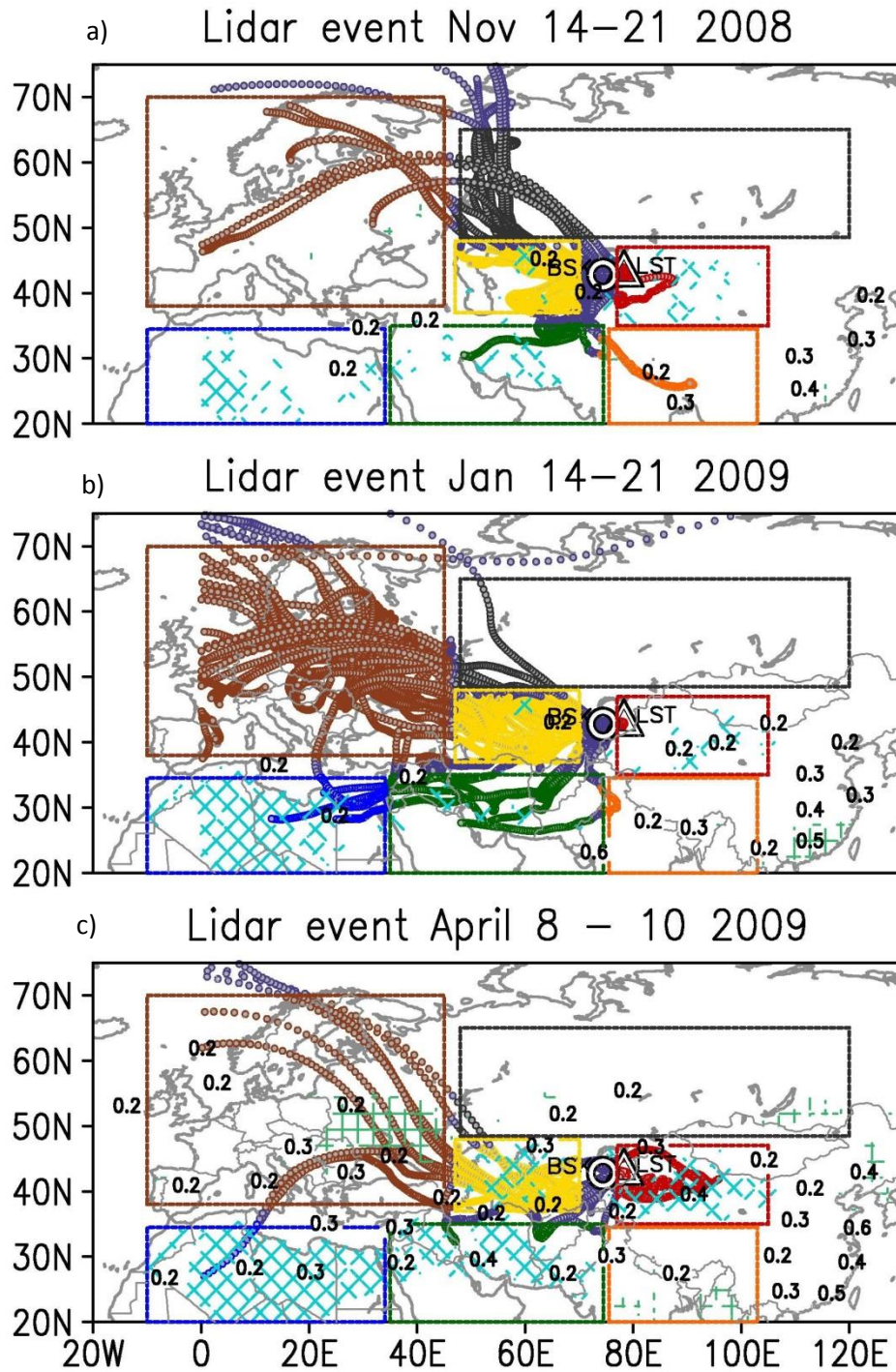


Fig. 15. Same as Fig. 14 but for November 2008, January 2009 and April 2009 (events 3, 4, 5 denoted in Fig. 13).

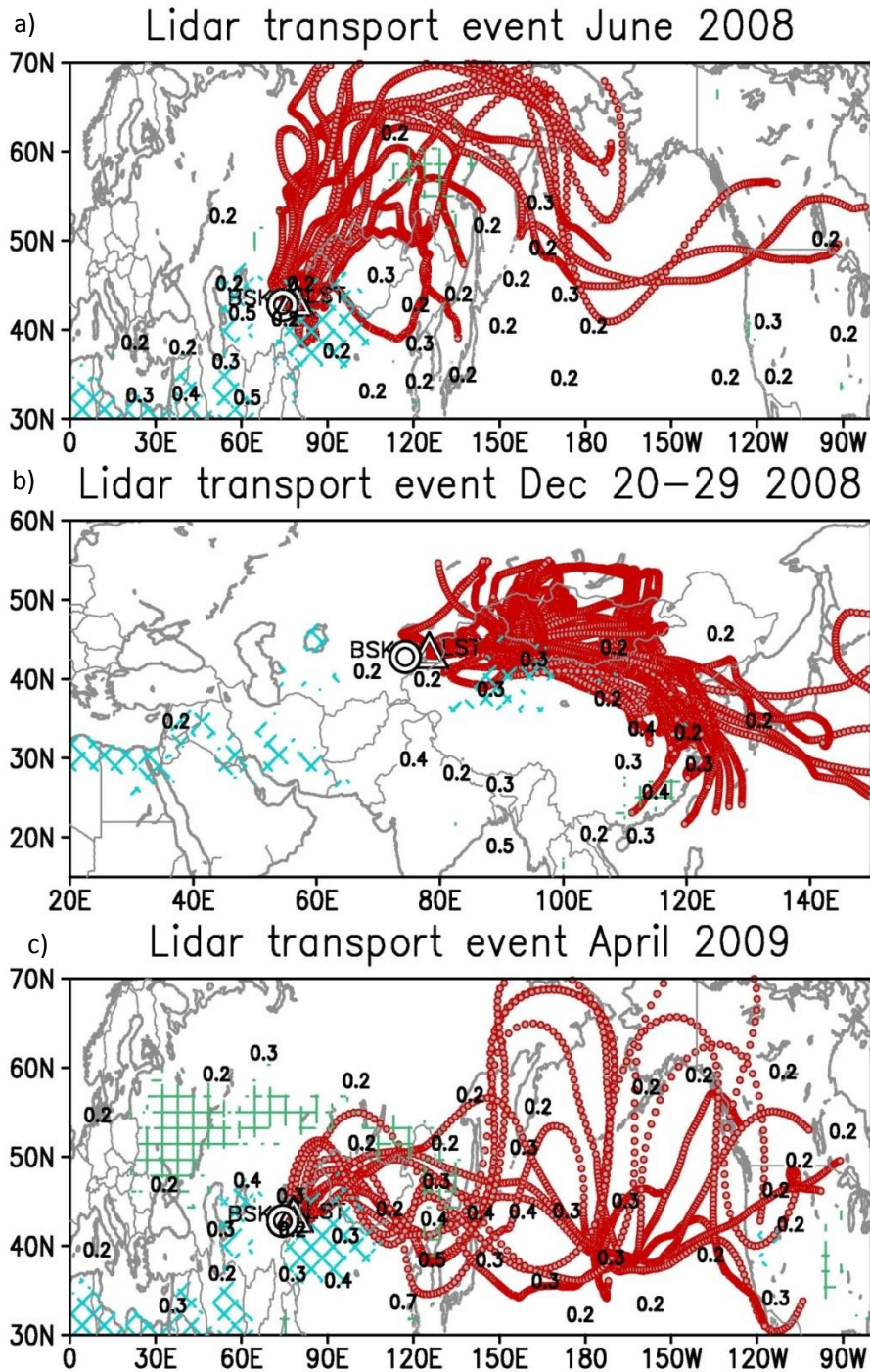


Fig. 16 Ten day air mass forward trajectories illustrating the seasonality in transport pathways out of CA for a) June 2008, b) December 2008, and c) April 2009. The blue diamond, green square hatched areas denote the natural dust and biomass burning emission sources while the number in black denote MODIS AOD contours, respectively, averaged over the event time

period and subsequent ten day time window. Lidar denotes the LST (Lidar Station Teplokluchenka) site.

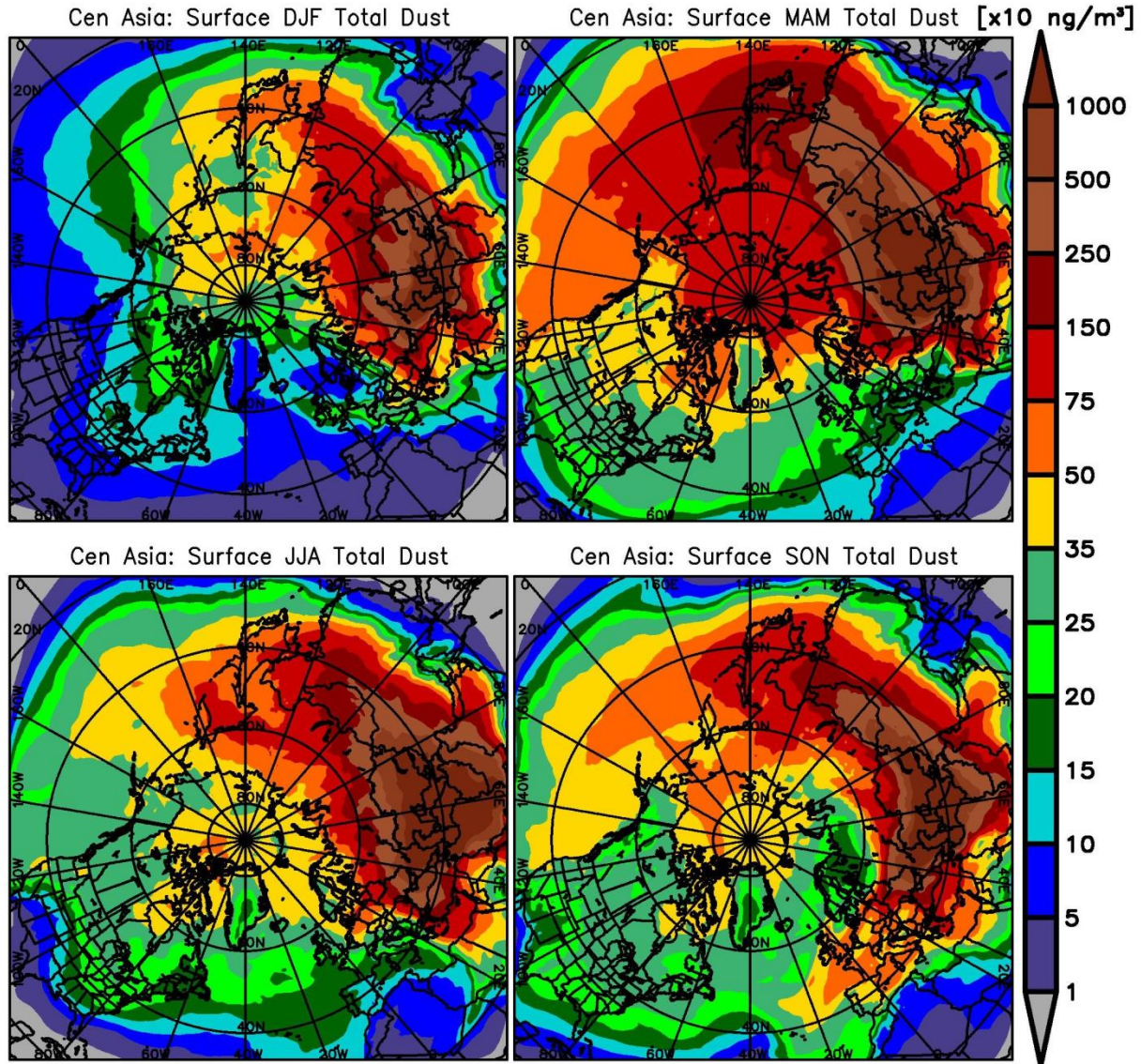


Fig. 17. Seasonally averaged surface total dust (PM₁₀) concentrations from Central Asia dust emissions. DJF (top left panel) denotes the average for the months of December, January and February. MAM (top right panel) denotes the average for months of March, April and May. JJA (bottom left panel) denotes the average for months of June, July and August while SON (bottom right panel) denotes average for months of September, October and November.

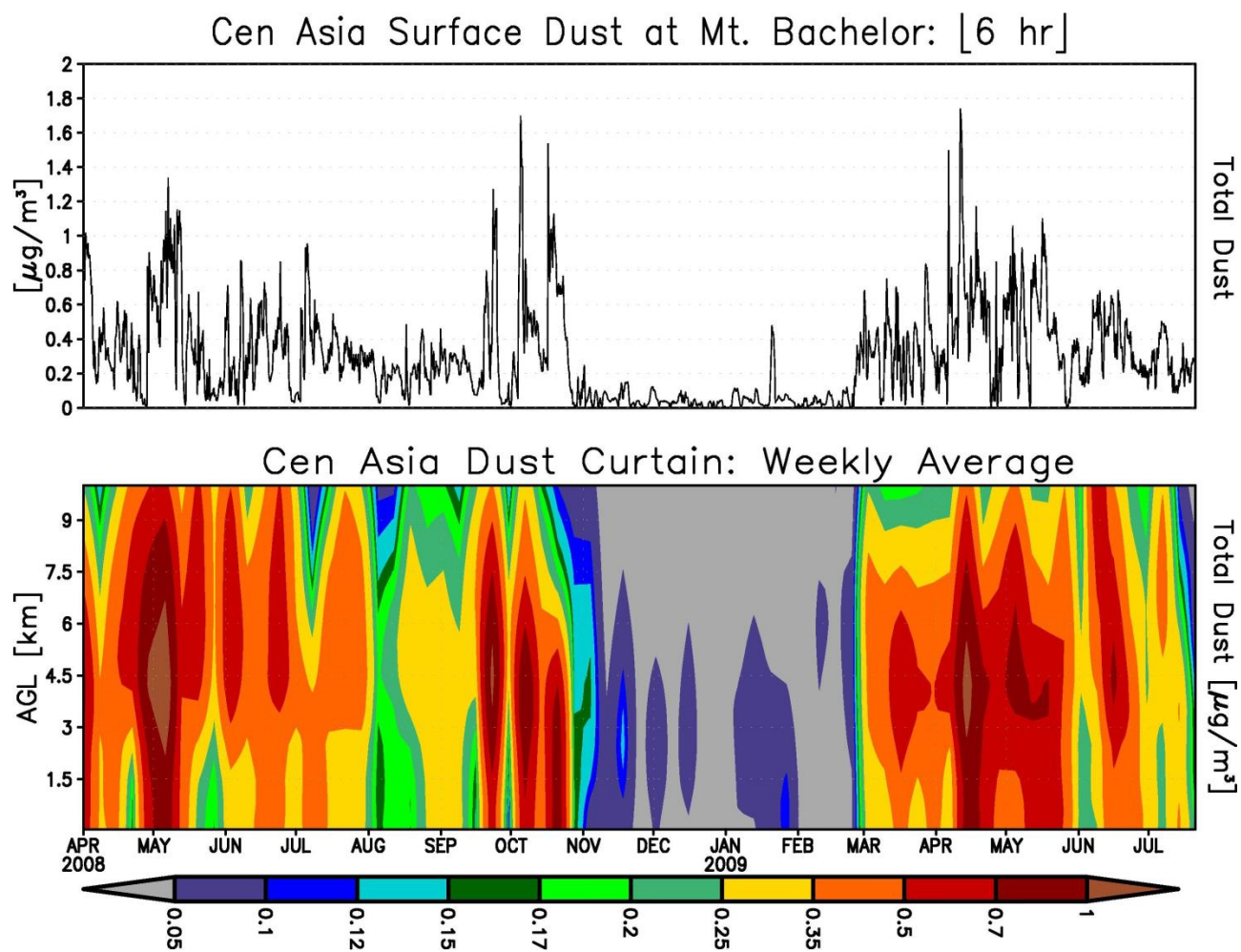


Fig. 18. Time series of predicted surface concentration at 6 h time step (top panel) and weekly averaged time altitude cross sections (bottom panel) of total dust (PM_{10}) from Central Asia dust emissions at Mt. Bachelor, Oregon.

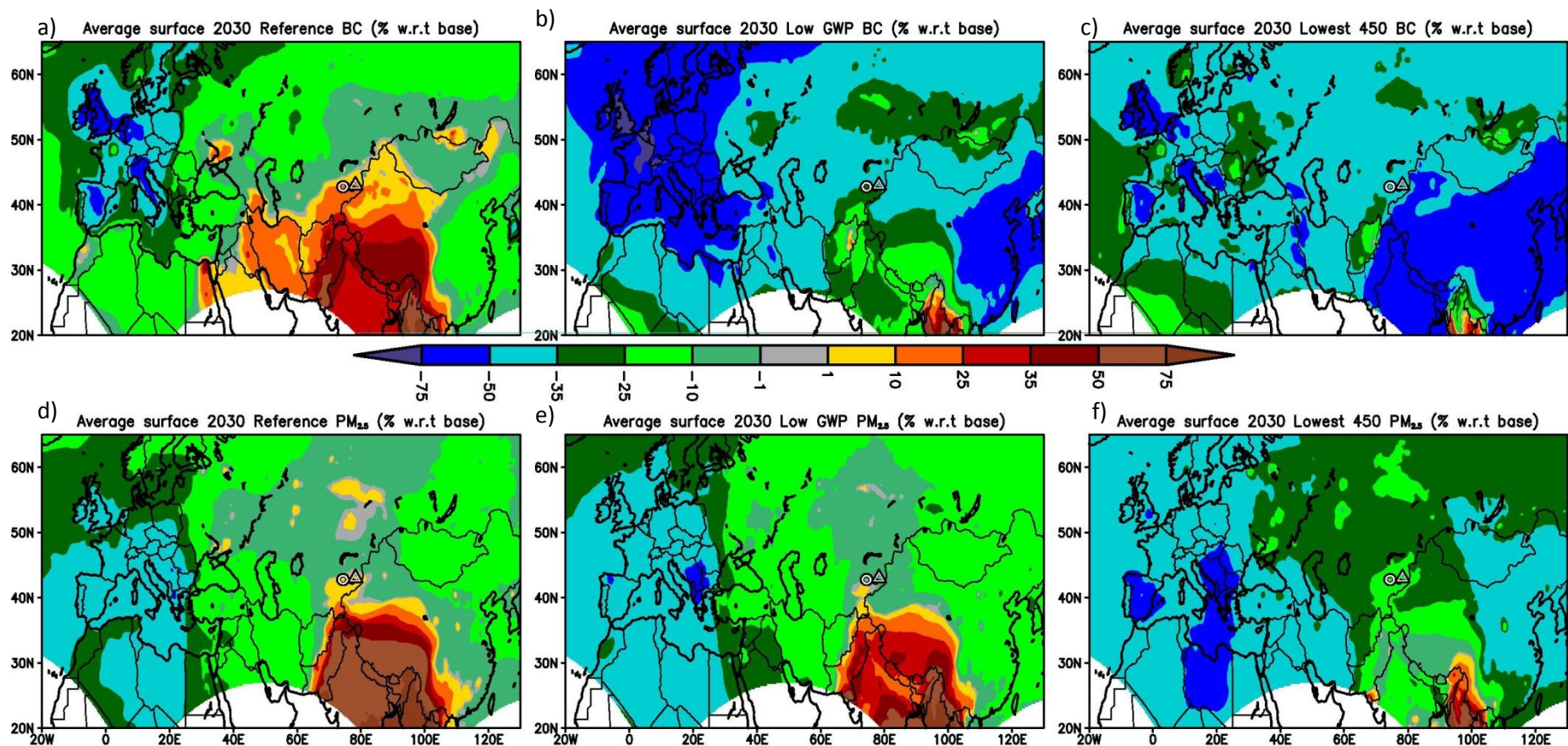


Fig. 19. Percent change in simulated period mean surface BC and PM_{2.5} concentrations for future 2030 emission scenarios relative to the base year (2005) a),d) reference 2030, a),e) BC measures (low) and c),f) BC (lowest) and greenhouse gas measures aimed at keeping CO₂ levels below 450 ppm. Refer to Sec. 2.3 for more details on emission scenarios.